6-4-2020

Hadronic Contributions to the Muon Anomalous Magnetic Moment using Lattice QCD

Cheng Tu
University of Connecticut - Storrs, serenetu@gmail.com

Hadronic Contributions to the Muon Anomalous Magnetic Moment using Lattice QCD

Cheng Tu, PhD

University of Connecticut, 2020

The hadronic vacuum polorization (HVP) contribution and long-distance hadronic light-by-light (HLbL) scattering contribution to the muon anomalus magnetic moment are evaluated by using lattice QCD. The HVP calculations are performed with $2 + 1 + 1$ flavors of HISQ fermions at the physical pion mass from three ensembles, generated by the MILC collaboration. In the long-distance part of the HLbL contribution, we replace the QCD, four-current connected Green's function from previous HLbL study with the product of two independent $\pi\gamma\gamma$ amplitudes, which are joined by an analytic, position space pion propagator. The calculations are performed with near physical pion mass on four different lattice ensembles, which are generated by RBC/UKQCD Collaboration.

Hadronic Contributions to the Muon Anomalous Magnetic Moment using Lattice QCD

Cheng Tu

B.S., Hebei University of Technology, 2013

M.S., University of Connecticut, 2020

A Dissertation

Submitted in Partial Fulfillment of the

Requirements for the Degree of

Doctor of Philosophy

at the

University of Connecticut

2020

2020

APPROVAL PAGE

Doctor of Philosophy Dissertation

Hadronic Contributions to the Muon Anomalous Magnetic Moment using Lattice QCD

Presented by

Cheng Tu, B.S., M.S.

Major Advisor _____

Thomas Blum

Co-Major Advisor _____

Luchang Jin

Associate Advisor _____

Gerald V. Dunne

University of Connecticut

2020

ACKNOWLEDGMENTS

I am very grateful to my advisor Prof. Thomas Blum, a respectable and responsible scholar. He bring me into this beautiful, challenging world of physics with his insightful knowledge and patience. Never forget the first time he took me to the BNL for a research meeting. It is my honor to have Prof. Blum supervise me on my entire PhD work.

I also would like to thank Prof. Luchang Jin, who is my co-advisor. He is smart, knowledgeable and young! He can always explain a complex concept in a simple way. Qlattice, a code lib for lattice calculation written by him, is super stable and make this work achievable.

I would like to thank Prof. Gerald V. Dunne, Prof. Alexander Kovner, Prof. Richard Jones, Prof. Philip Mannheim and many others, who provide well guided courses, from where I get solid physics fundamentals.

Finally, I would like to thank my family with their strong support these years. Especially thank to my wife Maxiao, who make me no longer feeling lonely.

Contents

List of Tables

List of Figures

Chapter 1

Introduction

The purpose of my study is to calculate the contribution from hadronic vacuum polarization (HVP) and π^0 contribution to the long-distance hadronic light by light (HLbL) to the muon magnetic moment by using Lattice QCD [9], which is a non-perturbative approach to solving QCD theory of quarks and gluons. Before going into details of this calculation, I would like to give a brief introduction to the background of the muon magnetic moment, the reason why it is so important for learning QCD and finding potential new physics.

A charged particle with half-integer intrinsic spin has a magnetic dipole moment defined as

$$\vec{\mu} = g_l \frac{e}{2m} \vec{s}, \tag{1.1}$$

where the l can be one of the charged leptons (e, μ, or τ) and g_l denotes the corresponding Landé g-factor. The 'anomalous' arise from the difference between g_l and the Dirac value 2. The leading order Feynman diagram of Fig. 1.1, which was first computed by Julian

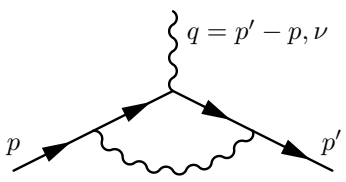

Figure 1.1: Leading order contribution to $g - 2$

Schwinger in 1948, gives the value of

$$\frac{\alpha}{2\pi} \ , \tag{1.2}$$

where the $\alpha = e^2/(4\pi)$ is the fine structure constant. Actually, an extremely precise evaluation of electron $g-2$ was achieved. In experiment side, we got 0.24 ppb, and even higher precision from the calculation to tenth-order QED contribution. Comparing between the experimental and theoretical results of electron $g-2$ provide one of the most precise way to determine the fine structure constant α. However, electron $g-2$ is not a good choice to study uncovered physics that is beyond standard model. New particles and interactions occur at very large energy scale Λ and their indirect effect at low energy suppressed by the ratio of $(m_e/\Lambda)^2$, making electron limited sensitive to new physics. Fortunately, there are two more particles in charged lepton family, μ and τ. Since the lifetime of τ is too short, the accurate measurement for its magnetic moment is very difficult, so the muon $g-2$ is a good choice to search new physics.

Table 1.1: Muon $g-2$ current status

	$a_\mu \times 10^{10}$	Group
QED [10]	$11\,658\,471.895 \pm 0.008$	Aoyama, et al, 2012
Electroweek [11]	15.4 ± 0.1	Gnendiger et al, 2013
HVP LO [12]	694.9 ± 4.3	FJ17
HVP NLO [12][13]	-9.84 ± 0.06	FJ17
HVP NNLO [13]	1.24 ± 0.01	FJ17
HLbL [14]	10.5 ± 2.6	FJ17
Standard Model	$11\,659\,181.3 \pm 4.0$	
Experiment(0.54 ppm) [15]	$11\,659\,208.9 \pm 6.3$	E821, The $g-2$ Collab.

In fact, the muon $g-2$ is one of the most precisely measured and the theoretically best investigated quantities in particle physics. The most precise experimental result right now is from Brookhaven National Laboratory [15] and the theory value disagrees by about $3-4$ standard deviations [16] (see Tab.1.1). The new experiment at Fermilab E989 which succeeds E821 is running and will announce their first results soon. The aim at Fermilab E989 [17] and J-PARC E34 [18] is to reduce the uncertainty by a factor of 4. Therefore, a

corresponding theoretical effort is necessary to pursue the increasing experimental precision. The theory error of the muon $g-2$ is dominated by hadronic contributions: the hadronic vacuum polarization (HVP) and hadronic light-by-light scattering (HLbL) which are in order of $\mathcal{O}(\alpha^2)$ and $\mathcal{O}(\alpha^3)$ respectively.

In Chapter 2, I will give a short introduction for lattice QCD, which is the technique we use for hadronic contribution computations. I will talk about how lattice QCD describe the partition function, gauge action and fermions. All-mode averaging (AMA) and Low-mode averaging (LMA) techniques for noise reduction are also shown in that section. In section 3, I report on the computation of the connected light quark vacuum polarization with $2+1+1$ flavors of highly improved staggered quark (HISQ) fermion at the physical point and its contribution to the muon $g-2$. In Chapter 4, I will discuss the position-space π^0 exchange contribution to the long-distance part of the HLbL contribution to the muon $g-2$.

Chapter 2

Lattice QCD

QCD is a theory describing strong interactions between quarks and gluons. Since the large coupling constant of such interactions in low energy region, one requires a non-perturbative method, and the lattice QCD is a tool to carry out such calculations. Lattice QCD provide a systematic way to study QCD non-perturbatively. It is a gauge field theory on 4d discrete Euclidean lattice spacetime, and quantized along the Feynman's path integral formalism. Since lattice QCD is just regularized QCD, no new parameters or field variables are introduced here.

2.1 Partition function

We start with the partition function, which can be written as,

$$Z = \int [dU] \prod_f [dq_f][d\bar{q}_f] e^{-S_g(U) - \sum_f S_f(q_f, \bar{q}_f, U)} \ , \tag{2.1}$$

where $S_g(U)$ is the gauge action in terms of SU(3) matrix U which represent gauge field, $S_f = \sum_f \bar{q}_f (D(U) + m_f) q_f$ is the fermion action and D denotes the Dirac operator, and m_f is the quark mass. Since the fermion field is represented as the anticommuting Granssmann

field, one can first integrate out the quark and antiquark fields,

$$Z = \int [dU] e^{-S_g(U)} \prod_f \det(D(U) + m_f). \tag{2.2}$$

An expectation value of an observable is represented as,

$$\langle O \rangle = \frac{1}{Z} \int [dU] O(S_q(U), U) e^{-S_g(U)} \prod_f \det(D(U) + m_f), \tag{2.3}$$

where $S_q = (D(U)+m_f)^{-1}$ is a quark propagator. Eq. (2.3) means that the observable can be obtained by integrating over gauge configuration U with the weight of $e^{-S_g(U)} \prod_f \det(D(U)+m_f)$. We can then apply the Monte Carlo importance sampling method to generate the gauge configurations with the probability of $e^{-S_g(U)} \prod_f \det(D(U)+m_f)$, and the physical quantity becomes

$$\langle O \rangle = \frac{1}{N_{\text{sample}}} \sum_i O(U_i). \tag{2.4}$$

2.2 Lattice fermions

In lattice QCD, how to discretize the fermion action is a huge problem. we start from the continuum fermion action, which is $S_f = \int d^4x \bar{\psi}(iD_\mu \gamma_\mu + m_f)\psi$, where $D_\mu = \partial_\mu + iA_\mu$ is the gauge-covariant derivative. The naive fermion discretization replace the derivative with a symmetric difference in the lattice,

$$D_\mu \psi(x) \to \frac{1}{2a}\big(U_\mu(x)\psi(x + a\hat{\mu}) - U_\mu^\dagger(x - a\hat{\mu})\psi(x - a\hat{\mu})\big), \tag{2.5}$$

where a is lattice spacing. The factors of $U_\mu(x)$ ensures that $D_\mu\psi(x)$ transform under gauge transformations in the same way as $\psi(x)$, so that the discretized version of fermion action is gauge invariant. This, however, suffers from the fermion doubling problem - in d dimensions it describe 2^d equivalent fermion fields in the continuum limit. Think about the inverse of

the free field propagator in momentum space with $U_\mu(x) = 1$,

$$S^{-1}(p) = m + \frac{i}{a}\sum_\mu \gamma_\mu \sin(p_\mu a), \tag{2.6}$$

which has 16 zeros in the limit $m \to 0$ within the Brillouin zone $\{-\pi/2, 3\pi/2\}$ when $p_\mu = 0$ and π. So the naive discritization of lattice fermions induces 16 degenerate types ("tastes") of fermions, but we only want to simulate one of them. We need to figure out some way of getting rid of the other 15 tastes.

2.2.1 Wilson fermions and staggered fermions

One way for dealing with the doubling problem is called Wilson fermions by adding the Wilson term propotional to $a\bar{\psi}\Delta\psi$ to the fermion action [19]. This term gives extra fifteen tastes at $p_\mu = \pi$ a mass of $\mathcal{O}(1/a)$, so they decouple in the continuum limit. The advantages of the Wilson fermions are their theoretical simplicity and relative low computational cost. However, the Wilson term break the chiral symmetry.

There is another way to reduce the number of the tastes, called "staggering" [20]. Staggered fermions χ are defined by the transformation,

$$\psi(x) = \Gamma_x \chi(x) \quad \bar{\psi}(x) = \bar{\chi}(x)\Gamma_x^\dagger \quad \Gamma_x = \gamma_1^{x_1}\gamma_2^{x_2}\gamma_3^{x_3}\gamma_4^{x_4}. \tag{2.7}$$

We can think of it as putting the four spin components of the Dirac spinor on different sites of the lattice and by applying such transformation, the action matrix can be diagonalized to

$$\sum_x \sum_{i=1,2,3,4} \eta_\mu(x)\bar{\chi_i}(D_\mu + m)\chi_i, \tag{2.8}$$

where $\eta_\mu(x) = (-1)^{\sum_{\nu<\mu} x_\nu}$. It shows that the spin compoments of χ are decoupled since the phase factor $\eta_\mu(x)$ depends only on the site index and direction and do not have spinor

index and one can therefor just keep one. In all, the fermion action can be written as,

$$S_s = \sum_{x,y} \bar{\chi}(x) M^S_{xy} \chi(y) \tag{2.9}$$

with the matrix M^S given by

$$M^S[U]_{x,y} = m\delta_{xy} + \frac{1}{2}\sum_{\mu} \eta_\mu(x)[U_\mu(x)\delta_{x,y-\mu} - U^\dagger_{x-\mu,\mu}\delta_{x,y+\mu}]. \tag{2.10}$$

The staggered fermions have the advantages of being somewhat faster to simulate than Wilson-like fermions, and they also preserve the chiral symmetry. The disadvantage is that they retain some of the doublers (3 for d = 4). The staggered action can be improved to reduce discretization errors. The "asqtad" action removes tree-level $\mathcal{O}(a^2)$ errors and highly improved staggered quark (HISQ) action [21], which we use for HVP calculation, further reduces discretization errors.

2.2.2 Domain wall fermions

In order to get exactly chiral fermion, we introduce the domain wall fermions. Instead of four dimensions, we can image the fermion lives in really five-dimension in which a scalar field m depend on only the fifth dimension s and the chiral fermion arise from the domain wall in the fifth dimension. To see this, let us start from a five dimension action in the continuum limit [22],

$$S = \int d^4x ds \bar{\psi}(x,s) \left(\sum_{\mu=1}^{5} \gamma_\mu \partial_\mu - m(s) \right) \psi(x,s) \tag{2.11}$$

where $m(s)$ is a step function

$$m(s) = \begin{cases} m_0 & s > 0 \\ 0 & s = 0 \\ -m_0 & s < 0 \end{cases} . \tag{2.12}$$

And the equation of motion of the fermion field gives,

$$\left(\sum_{\mu=1}^{5} \gamma_\mu \partial_\mu - m(s) \right) \psi(x, s) = 0. \tag{2.13}$$

For $\psi(x, s)$, taking separation of variables to $\psi(x, s) = \psi(x)\chi(s)$ and considering a massless single momentum field which is $\psi(x) = u(p)e^{ipx}$, after putting back to the equation (2.13), the following conditions must be satisfied [23],

$$\gamma_5 u(p) = \pm u(p) \tag{2.14}$$

$$\pm \partial_5 f(s) - m(s) f(s) = 0, \tag{2.15}$$

from which the solution is

$$f(s) = Ce^{\pm m_0 |s|}. \tag{2.16}$$

For $m_0 > 0$, $f(s)$ can only take the normalizable form $f(s) = Ce^{-m_0|s|}$ and at the same time $\gamma_5 u(p) = -u(p)$, which is a left handed massless spinor. Until now, we are focusing on infinite fifth dimension and continuous limit conditions. To move forward, it is useful to consider a periodic boundary conditions in the fifth dimension $\psi(x, -s_0) = \psi(x, s_0)$ and the mass function $m(s)$ has a domain wall kink at $s = 0$ and an anti-kink at $s = \pm s_0$. In this region, both left-handed and right handed spinor exist simultaneously, so in $s = 0$, right handed spinor still exit proportional to $e^{-|m_0|s_0}$, and the same for $s = \pm s_0$. In this case, at finite fifth dimension, there will always be some chiral symmetry breaking, and by coupling

different handed spinor, it will also cause a shift the mass, called a residual mass.

2.3 Low mode averaging and all mode averaging

One of the most important phase in lattice calculations is the construction of Euclidean correlation functions, and two-point correlation functions (used in HVP) typically rely on quark smearing. The statistical errors of correlation functions come from two sources. One is from the gauge field sampling, which can be decreased by enlarging the number of gauge configurations. Another one is measurement noise on each gauge configuration and increasing the number of independent measurements will reduce it. However the exact measurement in terms of the inverse of the Dirac operator with high numerical precision and small conjugate gradient (CG) stopping residual cost expensive computation resources. Fortunately, the accuracy of the high mode part of the propagator does not require a small stopping residual since this part converges fastest in the CG procedure. Such a property implies "sloppy" measurements using many source locations will yield a much smaller error than using exact measurements with fewer locations. All mode averaging (AMA) defines such unbiased estimator $O^{(\mathrm{imp})}$ of an observable O from approximate measurement $O^{(appx)}$ [24, 25, 26, 27, 28, 29, 3],

$$\left\langle O^{(\mathrm{imp})} \right\rangle = \left\langle \left(O - O^{(appx)} \right) \right\rangle + \frac{1}{N_G} \left\langle \sum_{g \in G} O^{(appx),g} \right\rangle , \tag{2.17}$$

where G denotes lattice symmetry transformation set and g is part of the set. For low mode averaging (LMA), one can just substitute an observable with lowest eigenmodes constructed propagators for $O^{(appx)}$. $O^{(appx)}$ should fluctuate closely with O and the cost to compute $O^{(appx)}$ needs to be smaller than O's. Furthermore, under a lattice symmetry transformation, $g \in G$, $O^{(appx)}$ should be covariant,

$$\left\langle O^{(\mathrm{appx})} \left[U^g \right] \right\rangle = \left\langle O^{(\mathrm{appx}),g} [U] \right\rangle . \tag{2.18}$$

To examine the details of the LMA and AMA, one can consider low-mode eigenvalues and eigenvectors of the Hermitian Dirac operator,

$$D_H \left|\lambda_i\right\rangle = \lambda_i \left|\lambda_i\right\rangle, (i = 1, 2, \ldots, N_{\text{eig}}) \tag{2.19}$$

$$0 < |\lambda_1| \leq |\lambda_2| \leq \cdots \leq \left|\lambda_{N_{\text{eig}}}\right| = \lambda_{\text{cut}} \,. \tag{2.20}$$

For most cases, low-mode is already a good approximation for observables, such as the single pion state for lighter fermion masses. For example, the low-mode approximation of a fermion propagator reads,

$$S_{LM} = \sum_{i=0}^{N_{eig}} \frac{\left|\lambda_i\right\rangle \left\langle\lambda_i\right|}{\lambda_i}. \tag{2.21}$$

However, for those quarks with heavier masses, low-mode approximation does not work so well. This is due to the high mode contribution to the propagator. To consider high mode parts ($|\lambda| > \lambda_{\text{cut}}$) and use limited computational resources, we introduce all-mode. A propagator for all-mode can be expressed as the exact low-mode part plus an undetermined coefficient $P_n \approx 1/\lambda$, which is a polynomial of degree n, applied to the subspace orthogonal to the low-mode eigenvectors [30],

$$S_{AM} = \sum_{i=0}^{N_{eig}} \frac{\left|\lambda_i\right\rangle \left\langle\lambda_i\right|}{\lambda_i} + P_n \left(1 - \sum_{i=1}^{N_{eig}} \frac{\left|\lambda_i\right\rangle \left\langle\lambda_i\right|}{\lambda_i}\right). \tag{2.22}$$

To obtain an approximate value for P_n, we usually use an iterative method like CG and set either the iteration numbers or CG residual stopping criterion. The low-modes can be eliminated easily from the starting vector of the CG (a procedure known as deflation), which then yields the high mode part.

In HVP calculation, we combine AMA and full-volume LMA as an improved estimator,

$$\langle O \rangle = \langle O \rangle_{\text{exact}} - \langle O \rangle_{\text{approx}} + \frac{1}{N} \sum_i \langle O_i \rangle_{\text{approx}} - \frac{1}{N} \sum_i \langle O_i \rangle_{\text{LM}} + \frac{1}{V} \sum_i \langle O_i \rangle_{\text{LM}} \,, \tag{2.23}$$

where N denotes the number source locations under symmetry transformation group and V is the number of full volume sites. This estimator dramatically decrease the errors coming from the low-mode with a balanced computation resources. The details are described in the next chapter.

Chapter 3

Lowest-order hadronic vacuum polarization contribution

The largest part of the hadronic contributions of a_μ comes from the leading order vacuum polarization, which is in order of $\mathcal{O}(\alpha^2)$. As we can see in Tab. 1.1, the theoretical result from the HVP contribution has the largest errors and this is the first case in which the effects of the strong interaction enter the determination of a_μ. Our computation use $2+1+1$ flavors of highly improved staggered quarks (HISQ) [21] at the physical point and we find $a_\mu^{ll}(\text{HVP}) = (659 \pm 20 \pm 5 \pm 5 \pm 4)$, where the errors are statistical and estimates of residual uncertainties from taking the continuum limit, scale setting and truncation of chiral perturbation theory. In this chapter, I will mainly talk about our lattice computation with the noise reduction technique AMA and LMA. Also the new hardware and modern computer technology make this work achievable. The second generation Xeon Phi processor from Intel provide powerful 512-bit vector units and AVX-512 single instruction multiple data (SIMD) instructions. I will explain some of the coding implementations in this work, which include several deep level optimizations by using those techniques.

3.1 Dispersion relation approach

The HVP contribution can be determined directly from measured cross section of e^+e^- annihilation into hadrons by using dispersion relations. Dispersion relations are a powerful non-perturbative tool by using the general analytic properties, which follow from causality and the use of Cauchy's theorem. By using dispersion relations, we can obtain the real part of an amplitude from the knowledge of the imaginary part which is often better accessible with optical theorem.

Starting from the direct consequence of the unitarity of the S-matrix: $S^\dagger S = 1$ and its expression written in terms of identity part and interaction part: $S = \mathbb{1} + iT$, we have

$$-i(T - T^\dagger) = T^\dagger T. \tag{3.1}$$

Applying above equation into the matrix element between two-particle states and inserting a complete set of intermediate states, we obtain

$$\begin{aligned}
&-i[\mathcal{M}(k_1k_2 \to p_1p_2) - \mathcal{M}^*(p_1p_2 \to k_1k_2)] \\
&\quad = \sum_n \Big(\prod_{i=1}^n \int \frac{d^3q_i}{(2\pi)^3} \frac{1}{2E_i} \Big) \langle \mathbf{p}_1\mathbf{p}_2|T^\dagger|\{\mathbf{q}_i\}\rangle\langle\{\mathbf{q}_i\}|T|\mathbf{k}_1\mathbf{k}_2\rangle \\
&\quad = \sum_n \Big(\prod_{i=1}^n \int \frac{d^3q_i}{(2\pi)^3} \frac{1}{2E_i} \Big) \mathcal{M}^*(p_1p_2 \to \{q_i\})\mathcal{M}(k_1k_2 \to \{q_i\})(2\pi)^4\delta^{(4)}(k_1 + k_2 - \sum_i q_i).
\end{aligned} \tag{3.2}$$

When we set $p_i = k_i$ and apply the relation between S-matrix elements and cross sections, we can get the standard form of the optical theorem

$$\mathrm{Im}\mathcal{M}(k_1k_2 \to k_1k_2) = 2E_{\mathrm{cm}}p_{\mathrm{cm}}\sigma_{\mathrm{tot}}(k_1k_2 \to \text{anything}), \tag{3.3}$$

where E_{cm} is the total center-of-mass energy and p_{cm} is the momentum of either particle in the center-of-mass frame. This relation shows the connection between the imaginary part of

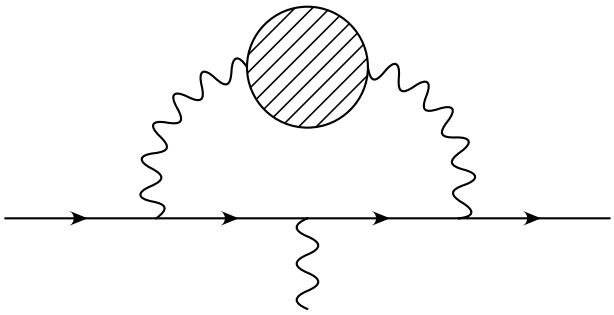

Figure 3.1: The lowest order hadronic contribution to the muon anoumalous magnetic moment.

the scattering amplitude and the total cross section for production of all final states. To the HVP, it becomes

$$\sigma(e^+e^- \to \text{hadrons}) = -\frac{4\pi\alpha}{s}\text{Im}\Pi(s). \tag{3.4}$$

Then for dispersion relations, we consider an analytic function $f(s)$ and integral representation by Cauchy's theorem,

$$f(s) = \frac{1}{2\pi i}\int_\gamma \frac{ds' f(s')}{s'-s}, \tag{3.5}$$

where s is inside the contour of γ, which does not cross any singularities. Using the same techniques to the HVP, we have

$$\begin{aligned}\Pi(s) - \Pi(0) =& \frac{s}{2\pi i}\int_\gamma \frac{\Pi(s')}{s'(s'-s)}ds' \\ =& \frac{s}{2\pi i}\int_{4M_\pi^2}^\infty \frac{\text{Disc}\Pi(s')}{s'(s'-s-i\epsilon)}ds' = \frac{s}{\pi}\int_{4M_\pi^2}^\infty \frac{\text{Im}\Pi(s')}{s'(s'-s-i\epsilon)}ds',\end{aligned} \tag{3.6}$$

where the relation of $\text{Disc}\Pi(s') = 2i\text{Im}\Pi(s')$ can be proved by the Schwartz reflection principle. Combining with Eq. (3.3), we can have a semi-phenomenological approach using experimental data.

3.2 Theoretical framework

We begin with the computation of loop graph in perturbation theory of the vertex function without hadronic contribution. After applying Feynman rules and taking the limit $q^2 \to 0$, the a_μ from the contribution of the diagram in Fig 3.1 reads

$$a_\mu = e^2 i \int \frac{d^4k}{(2\pi)^4} \frac{1}{[(p-k)^2 + m_\mu^2 - i\epsilon]^2} \frac{1}{k^2 - i\epsilon} \Big(\frac{16(p\cdot k)^2}{3m_\mu^2} + \frac{4}{3}k^2 + 4(p\cdot k) \Big) \tag{3.7}$$

where p is the momentum of the muon. The next step is that the Wick rotation into Euclidean space can be applied to the entire integration. After performing the angular integrations and analytically continuing $p^2 \to -m_\mu^2$ on shell for the external momenta, what is left is the integration of $K^2 = 0 \to \infty$ [31, 32, 33],

$$a_\mu = \frac{\alpha}{\pi} \int_0^\infty dK^2 \frac{m_\mu^2 K^2 Z^3 (1 - K^2 Z)}{1 + m_\mu^2 K^2 Z^2} = \frac{\alpha}{\pi} \int_0^\infty dK^2 f(K^2), \tag{3.8}$$

where

$$Z = -\frac{K^2 - \sqrt{K^4 + 4m_\mu^2 K^2}}{2m_\mu^2 K^2}. \tag{3.9}$$

As we can see, the integrand depend on K^2, and more importantly the HVP loop also only depend on K^2, so we can directly insert the HVP contribution into Eq. (3.8). We get

$$a_\mu^{\mathrm{HVP}} = 4\alpha^2 \int_0^\infty dq^2 f(q^2) \hat{\Pi}(q^2), \tag{3.10}$$

where $\hat{\Pi}(q^2)$ is the subtracted hadronic vacuum polarization, $\hat{\Pi}(q^2) = \Pi(q^2) - \Pi(0)$. The relation of $\Pi(q^2)$ and the vacuum polarization tensor $\Pi^{\mu\nu}(q)$ can be found through the Lorentz invariance and the Ward identity,

$$\Pi^{\mu\nu}(q) = (q^2 g^{\mu\nu} - q^\mu q^\nu)\Pi(q^2). \tag{3.11}$$

In lattice QCD, the vacuum polarization tensor $\Pi^{\mu\nu}(q)$ can be computed directly on a Euclidean space-time from the Fourier transform of the two-current function,

$$\begin{aligned}
\Pi^{\mu\nu}(q) &= \int d^4x\, e^{iqx}\langle j^\mu(x) j^\nu(0)\rangle & (3.12)\\
&= \Pi(q^2)(-q^\mu q^\nu + q^2\delta^{\mu\nu}), & (3.13)\\
j^\mu(x) &= \sum_i Q_i \bar{\psi}_i(x)\gamma^\mu\psi_i(x), & (3.14)
\end{aligned}$$

where $j^\mu(x)$ is the electromagnetic current with Lorentz and gauge symmetries, and Q_i is the quark electric charge in units of the electron charge e.

It is convenient to write a_μ in a time-momentum representation [34]. All we need to do is interchanging the order of the Fourier transform and momentum integrals in Eqs. 3.10 and 3.12.

$$a_\mu^{\rm HVP}(T) = \sum_{t=-T/2}^{T/2} w(t)C(t) = 2\sum_{t=0}^{T/2} w(t)C(t), \tag{3.15}$$

where

$$\begin{aligned}
C(t) &= \frac{1}{3}\sum_{\vec{x},i}\langle j^i(\vec{x},t) j^i(0)\rangle, & (3.16)\\
w(t) &= 4\alpha^2\int_0^\infty d\omega^2 f(\omega^2)\left[\frac{\cos\omega t - 1}{\omega^2} + \frac{t^2}{2}\right]. & (3.17)
\end{aligned}$$

We often write the weight term $\omega(t)$ with lattice version of the Euclidean momentum [3],

$$\hat{w}(t) = 4\alpha^2\int_0^\infty d\omega^2 f(\omega^2)\left[\frac{\cos\omega t - 1}{(2\sin(\omega/2))^2} + \frac{t^2}{2}\right]. \tag{3.18}$$

Note the cosine term in Eqs. 3.17 and 3.18 come from the double subtraction [34, 35, 36] to avoid a statistical noise problem for small momenta.

$$\Pi(q^2) - \Pi(0) = \sum_t \left(\frac{\cos qt - 1}{q^2} + \frac{1}{2}t^2\right) C(t), \tag{3.19}$$

where $t^2/2$ ensure that $\hat{\Pi}(q^2 = 0) = 0$ is satisfied "configuration-by-configuration" and the leading finite size correction is killed by the "-1" arises since $\Pi^{\mu\nu}(q^2)$ does not go to 0 when $q^2 \to 0$ when the lattice is finite [34]. These terms do not break the Ward identity and are allowed by the lattice symmetries [34, 36].

We consider the finite-volume effects, taste symmetry breaking, and pion mass corrections to the lattice calculation. The finite-volume corrections are obtained by taking the difference between infinite-volume and finite-volume results in chiral perturbation theory (ChPT) to the next-to-leading order (NLO) and next-to-next-leading order (NNLO) respectively. Taste-breaking effects are obtained similarly by differences between results computed with the Goldston pion mass and the average of contributions for each taste pion. The NLO, taste breaking and NNLO corrections read [37],

$$\Delta a_\mu^{\rm HVP} = \begin{cases} 15.6 \times 10^{-10}, & L/a = 96 \\ 6.9 \times 10^{-10}, & L/a = 64 \\ 2.1 \times 10^{-10}, & L/a = 48 \end{cases} \tag{3.20}$$

$$\Delta_{\rm tast}\, a_\mu^{\rm HVP} = \begin{cases} 9.5 \times 10^{-10}, & L/a = 96 \\ 34.2 \times 10^{-10}, & L/a = 64 \\ 51.6 \times 10^{-10}, & L/a = 48 \end{cases} \tag{3.21}$$

$$\Delta a_\mu^{\rm HVP,NNLO} = \begin{cases} 9.13 \times 10^{-10}, & L/a = 96 \\ 9.01 \times 10^{-10}, & L/a = 64 \\ 7.40 \times 10^{-10}, & L/a = 48 \end{cases} \tag{3.22}$$

3.2.1 AMA and LMA procedures

We have limitations of the computation resources, and one of the most expensive part of the computation is the computation of the quark propagator, which can be also thought as inverse of the Dirac operator. The AMA and LMA noise reduction techniques are applied

in the lattice computation. The combined AMA and full-volume LMA improved estimator is given by [24, 25, 26, 27, 28, 29, 3]

$$\langle O \rangle = \langle O \rangle_{\text{exact}} - \langle O \rangle_{\text{approx}} + \frac{1}{N}\sum_i \langle O_i \rangle_{\text{approx}} - \frac{1}{N}\sum_i \langle O_i \rangle_{\text{LM}} + \frac{1}{V}\sum_i \langle O_i \rangle_{\text{LM}}. \quad (3.23)$$

In AMA (the first three terms in Eq. 3.23), we firstly pick up small amount of points that we can compute exact propagators and use them to find the correlation function. Every propagator start from selected points to every other points in the lattice are computed to a high numerical precision with conjugate gradient stopping residual 10^{-8}. We subtract off the approximate estimate of the correlation function with the exact same points with what we do the exact calculation. Then we add back the approximate calculation again which is much cheaper compare to exact calculation on much more points in the lattice. The AMA is good for most of the lattice calculation, it turns out that is not good enough especially for the long tail of the HVP, so we want add in the LMA part, which is very effective in this case. We compute low mode part of the inverse of the Dirac operator for full volume. As in the last two terms of the Eq. 3.23, in addition to the AMA correlation function, we subtract off the LMA part with the points already in the AMA part and add back in the full volume average of the LMA calculation which has much smaller statistical error. The number of configurations in each lattice ensemble are shown in Tab. 3.1.

m_π (MeV)	a (fm)	size	L (fm)	$m_\pi L$	LM	AMA srcs	measurements (approx-exact-LMA)
133	0.12121(64)	$48^3 \times 64$	5.82	3.91	3000	$4^3 \times 4$	26-26-26
130	0.08787(46)	$64^3 \times 96$	5.62	3.66	3000	$4^3 \times 4$	36-36-40
134	0.05684(30)	$96^3 \times 192$	5.46	3.73	2000	$3^3 \times 8$	22-22-23

Table 3.1: Gauge field ensemble parameters [1]. "LM" is the number of low-modes of the preconditioned Dirac operator. "AMA srcs" is the number of approximate point source propagators on each configuration which are spread uniformly over several time slices. The number of exact point source propagators per configuration is eight for each ensemble. The number of configurations used for approximate, exact, and LMA measurements in this study are given in the last column.

3.2.2 Staggered Dirac operator and its low-mode structure

We use the highly improved staggered quarks (HISQ) [21] fermion Dirac operator minus the three-hop Naik term. In this section we will give the low-mode structure of the staggered fermion. The staggered Dirac operator in even odd ordering can be written like this,

$$M \begin{pmatrix} n_o \\ n_e \end{pmatrix} = \begin{pmatrix} m & M_{oe} \\ M_{eo} & m \end{pmatrix} \begin{pmatrix} n_o \\ n_e \end{pmatrix} = (m + i\lambda_n) \begin{pmatrix} n_o \\ n_e \end{pmatrix}, \tag{3.24}$$

where m is the quark mass and M_{oe} hops quarks from even to odd sites,

$$n_e = \frac{-i}{\lambda_n} M_{eo} n_o, \tag{3.25}$$

where $m + i\lambda$ and (n_0, n_e) are the eigenvalue and eigenvector of the Dirac operator respectively. In practice, by applying Lanczos algorithm, we use the preconditioned operator $M^\dagger M$ to compute eigenvectors (n_o, n_e) with squared magnitude eigenvalue,

$$\begin{pmatrix} m & -M_{oe} \\ -M_{eo} & m \end{pmatrix} \begin{pmatrix} m & M_{oe} \\ M_{eo} & m \end{pmatrix} \begin{pmatrix} n_o \\ n_e \end{pmatrix} = \tag{3.26}$$

$$\begin{pmatrix} m^2 - M_{oe}M_{eo} & 0 \\ 0 & m^2 - M_{eo}M_{oe} \end{pmatrix} \begin{pmatrix} n_o \\ n_e \end{pmatrix} = (m^2 + \lambda_n^2) \begin{pmatrix} n_o \\ n_e \end{pmatrix}. \tag{3.27}$$

Since the eigenvalues come in $\pm$ pairs for the staggered operator, if one has the eigenvector $n_+ = (n_0, n_e)$ with positive eigenvalue λ_n, one automatically has another eigenvector $n_- = (-n_0, n_e)$ with eigenvalue with minus sign $-\lambda_n$,

$$\begin{pmatrix} m & M_{oe} \\ M_{eo} & m \end{pmatrix} \begin{pmatrix} -n_o \\ n_e \end{pmatrix} = (m - i\lambda_n) \begin{pmatrix} -n_o \\ n_e \end{pmatrix}. \tag{3.28}$$

A spectral decomposition of the low-mode part of the quark propagator writes,

$$M^{-1}_{x,y} = \sum_{n}^{N_{\rm low}} \left(\frac{\langle x|n_+\rangle\langle n_+|y\rangle}{m+i\lambda_n} + \frac{\langle x|n_-\rangle\langle n_-|y\rangle}{m-i\lambda_n} \right) , \tag{3.29}$$

where $N_{\rm low}$ is the number of low modes.

We employ a conserved current in our computation which reads,

$$J^{\mu}(x) = -\frac{1}{2}\eta_{\mu}(x) \left(\bar{\chi}(x+\hat{\mu})U^{\dagger}_{\mu}(x)\chi(x) \ + \ \bar{\chi}(x)U_{\mu}(x)\chi(x+\hat{\mu}) \right) , \tag{3.30}$$

where U_μ are the gauge links for gauge invariance, $\chi(x)$ are the single spin component staggered fermion fields and $\eta(x)$ arise from the spin diagonalization of the fermion action. Combining with the Eq. (3.29), the low-mode structure of the two-point current-current correlation function then becomes

$$\begin{aligned} 4\sum_{\vec{x},\vec{y}} \langle J_{\mu}(t_x,\vec{x})J_{\nu}(t_y,\vec{y})\rangle &= -\sum_{m,n}\sum_{\vec{x},\vec{y}} \frac{1}{\lambda_m\lambda_n} \\ &\left(\Lambda^{\dagger}_{\mu}(x)_{mn}\Lambda^{\dagger}_{\nu}(y)_{nm} + \Lambda^{\dagger}_{\mu}(x)_{mn}\Lambda_{\nu}(y)_{nm} \right. \\ &\left. +\Lambda_{\mu}(x)_{mn}\Lambda^{\dagger}_{\nu}(y)_{nm} + \Lambda_{\mu}(x)_{mn}\Lambda_{\nu}(y)_{nm} \right) , \end{aligned} \tag{3.31}$$

where λ_n is short for $m \pm i\lambda_n$ with eigenvector ordering $\lambda_0, -\lambda_0, \lambda_1, -\lambda_1, \ldots, \lambda_{N_{\rm low}}, -\lambda_{N_{\rm low}}$, and the sums of labels m and n run up to $2N_{\rm low}$. $(\Lambda_\mu(t))_{n,m}$ is what we called meson fields,

$$(\Lambda_{\mu}(t))_{n,m} = \sum_{\vec{x}} \langle n|x\rangle\eta_{\mu}(x)U_{\mu}(x)\langle x+\mu|m\rangle(-1)^{(m+n)x+m}, \tag{3.32}$$

where the factor $(-1)^{(m+n)x+m}$ arise from the odd sites sign difference between n_+ and n_-. $(\Lambda_\mu(t))_{n,m}$ is the building block for the LMA part of the lattice computation and take the majority of the computation resources. The low-mode eigenvectors are also used to deflate the CG for quark propagators.

3.3 Computational Details

New hardware and techniques in computer make this work achievable. In 96^3 ensemble, the eigenvectors are tremendously large, about 3.8 terabytes (TB) per configuration, which is larger than the capacity of any single server node. Remember this is only the read in data and we need to compute odd sites of the eigenvectors which should also be kept in the memory during running time in order to find meson fields. Message passing interface (MPI) is widely used in lattice calculations, which provide a parallel way to manipulate huge amounts of data. Eigenvectors are split down into sub-volumes and each node takes one of the sub-volumes. In most of the running time, the meson fields can be computed in local node, except ones depend on the sites located in the boundary between two sub-volumes, which should be transferred through MPI. In order to take advantage the power of multi-core processor in each node, we use OpenMP to enable the multi-threading and each thread is assigned to one core. Since each of the meson fields is independent, the computation of each field can be distributed into different thread with a shared memory and each thread will take an amount of computation tasks to be load balanced. For most of the lattice calculation case, MPI and multi-threading are good enough. However, due to the large amount of site and number of the eigenvectors in 96^3 ensemble, making it a challenge to be computed in a reasonable running time with the current hardware set up. We need to push forward to find a deeper optimization way.

Luckily the second generation Knights Landing Xeon Phi processor provides 512-bit vector units and supports AVX-512 SIMD instructions, which make more room to do optimizations. The SIMD part of the code is inspired by Grid, which is a next generation data parallel C++ QCD library [38]. SIMD stands for 'single instruction, multiple data', which can perform the same operation on multiple data points simultaneously. The width of the vector unit denotes the data capacity, which is used for SIMD instruction like addition, multiplication etc. In our case, each 512-bit vector unit is capable of containing 8 complex values in single float precision. We implement SIMD vectorization on the meson fields, which

take the majority of the running time. In order to fully use the width of the vector units, every 8 sites of the eigenvectors are grouped as one SIMD computation unit to fill out the vector unit capacity. After using the SIMD technology, our program boost up to about 4 times faster than those without it.

As everyone knows continuous digits are approximately stored in several bits in a computer as floating-point numbers. In some cases, we need to take care about the precision when applying multiple multiplication or division operations. In Eq. 3.31 of this work, the magnitudes of eigenvalues are small in low-modes and we find that the order of the divisions of the eigenvalues, which can be taken place before or after the summation over sites, does impact the precision of final results. We choose to do the divisions after the sites summation since the precision errors will accumulate during the summation.

3.4 Results

The three lattice ensembles generated by the MILC collaboration that are used in our study are listed in Tab. 3.1. They have approximately the same physical pion mass and physical extent, $L \sim 5.5 - 5.8$ fm. The numbers of low modes used in the low-mode average and to deflate the conjugate gradient are also presented in Tab. 3.1. Due to the computer cluster memory capacity limitations, we use 2×2000 low mode in 96^3 ensemble, comparing to 2×3000 in other two ensembles. As you can see from Fig. 3.2 the full volume low-mode has large noise reduction effect on 48^3 and 64^3 ensembles, but in 96^3 ensemble, the LMA is not as effective due to the smaller number of low modes.

The bounding method [3, 2] on the correlation function is also applied in the time-integration in order to reduce further statistical errors. We define the upper and lower bound of the two-point correlation function as, for $t \leq T$, $C^{\mathrm{b}}(t) = C(t)$, and for $t > T$, $C^{\mathrm{b}}(t) = 0$ (lower bound) and $C^{\mathrm{b}}(t) = C(T)e^{-E_0(t-T)}$ (upper bound), where $E_0 = 2\sqrt{m_\pi^2 + (2\pi/L)^2}$. The E_0 denotes the two-pion energy state. By using this method, we do not have to sum

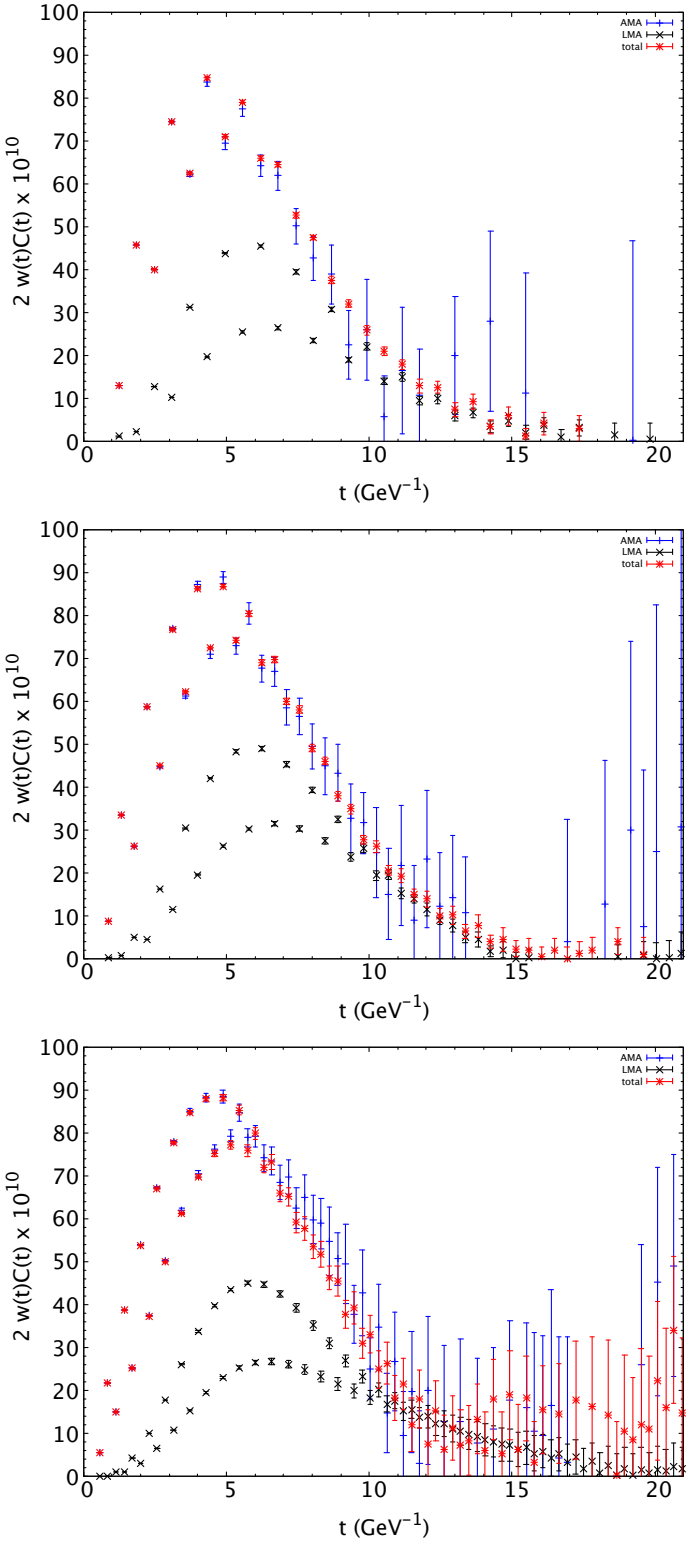

Figure 3.2: The summand in Eq. (3.15) for each ensemble in Tab. 3.1 (from top, coarsest to finest). Total (red stars) refers to the sum in Eq. (3.23). Also shown are the low-mode (black crosses) and AMA (blue plusses) contributions. Odd-parity, excited state oscillations intrinsic to staggered fermions are readily apparent.

over the whole range of time slices to compute $a_\mu^{\rm HVP}$, which contain the noisy long-distance tail. Instead, an estimate of $a_\mu^{\rm HVP}$ can be got from the overlap between two bounds in large T. Figure 3.3 shows the overlap we have chosen, which ranges for the 48^3 and 64^3 ensembles are $2.7 - 3.2$ fm and 96^3 ensemble $2.6 - 2.8$ fm. The statistical errors on the averages are computed using the jackknife method.

The lattice results of $a_\mu^{\rm HVP}$ from w and $\hat{w}$ weights in three ensembles are presented in Tab. 3.2. The bounding method helps to reduce the errors especially in 96^3 ensemble. We choose the "averaging window" based on the large overlap between upper and lower bounds and avoid the large fluctuations in the data at long times.

a (fm)	total (w)	total ($\hat{w}$)
0.12121(64)	562.1(8.4)	545.8(8.4)
0.08787(46)	594.8(10.4)	584.8(10.4)
0.05684(30)	623.1(27.5)	617.8(27.0)

Table 3.2: HVP contributions to the muon anomaly, in units of 10^{-10}. "total" refers to the bounding method described in the text, and w ($\hat{w}$) refers to the use of the weight given by Eq. (3.17) (Eq. (3.18)) in Eq. (3.15).

As we discuss above, we apply NLO, taste breaking effect and NNLO finite volume corrections to the lattice results. Firstly, NLO correction, taste breaking effect and the mistuning of the pion mass are applied for each ensemble respectively. Then after extrapolating to the continuum limit in a^2 ansatz from three ensembles, we add in the result of the average of the NNLO corrections. In Tab. 3.3, The second column shows the pure lattice results. The third and fourth columns are the values including NLO finite volume plus taste corrections respectively. Based on the fact that their continuum limits should agree with each other, we can estimate the systematic error from their difference, which equals to one-half of the difference, 4.8×10^{-10}. The fifth column gives the values by adding the pion mass retuning to the fourth column. The systematic error associated with the mistuning has been estimated by the spread of 5.1×10^{-10} between three values from extrapolating the NLO corrected $a_\mu^{\rm HVP}$. In the end, we apply the averaged NNLO correction of 8×10^{-10} with a ChPT error

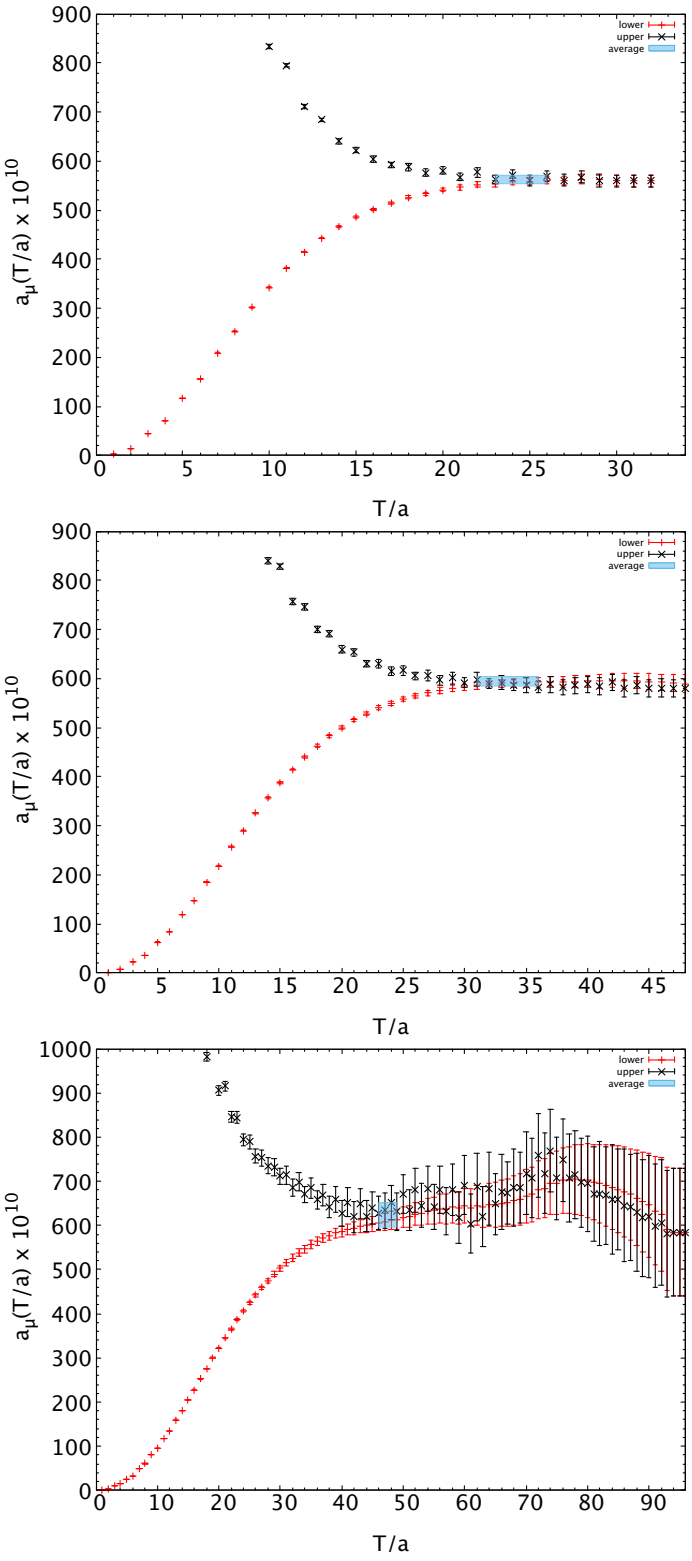

Figure 3.3: Bounding method for total contribution to the muon anomaly, using the weighting function w. 48^3 (top), 64^3 (middle), and 96^3 (bottom) ensembles. T/a is the time slice where $C(t)$ switches over from the calculated value to the analytic value giving the upper (black crosses) or lower (red plusses) bound. The blue shaded area indicates our averages.

of 4×10^{-10} to the result, so the final value reads:

$$(659 \pm 20 \pm 5 \pm 5 \pm 4) \times 10^{-10} = 659(22) \times 10^{-10}, \tag{3.33}$$

where the error 20 is statistical and the rest are systematic errors from continuum limit, pion mass mistuning and ChPT error respectively. The total error in the right hand side in the equation is computed by adding the individual errors in quadrature.

a (fm)	lattice value	FV corr.	FV + taste corr.	FV+taste+m_π corr.
0.12121(64)	562.1(8.4)	564.2(8.4)	615.8(8.4)	613.6(8.4)
0.08787(46)	594.8(10.4)	601.7(10.4)	635.9(10.4)	630.2(10.4)
0.05684(30)	623.1(27.5)	638.7(27.5)	648.2(27.5)	647.1(27.5)
0		648.3(20.0)	657.9(20.0)	651.1(20.1)

Table 3.3: HVP contributions to the muon anomaly, in units of 10^{-10}, including corrections computed in chiral perturbation theory. The second column repeats the second column of Table 3.2, the third column includes the finite-volume corrections of Eq. (3.20), while the fourth column also includes the infinite-volume taste corrections of Eq. (3.21). The fifth column adjusts the values shown in the fourth column to a common pion mass of 135 MeV using NLO ChPT, as described in the text. Continuum extrapolated values of each column are shown in the last row. The weighting function w has been used throughout.

3.5 Comparison with other results

We compare our result to other groups and collaborations. The FNAL/MILC/HPQCD published their recent updated computation of the $a_\mu^{\rm HVP}$. Our result 659(22) is consistent with their quoted value, 630.1(8.3), but larger. They used the same physical mass HISQ ensembles as we use here. The difference is that they used local-local current correlation functions and they applied brute-force computations on 1000's of configurations to control statistical errors. In the same lattice spacing, they got 580(7), 605(7) and 608(14) with statistical errors compared to the values in the second column of Tab. 3.2. Those values need not agree precisely due to the difference of the lattice spacing errors in the valence quark sector, but they should agree in the continuum and finite-volume limits. Another large part

of the difference comes from the NNLO ChPT with our quote 8×10^{-10}, comparing their model estimation range from -4×10^{-10} to -10×10^{-10} of the ensembles. Fig. 3.4 shows the recent results from other groups, and our result is consistent within errors with others.

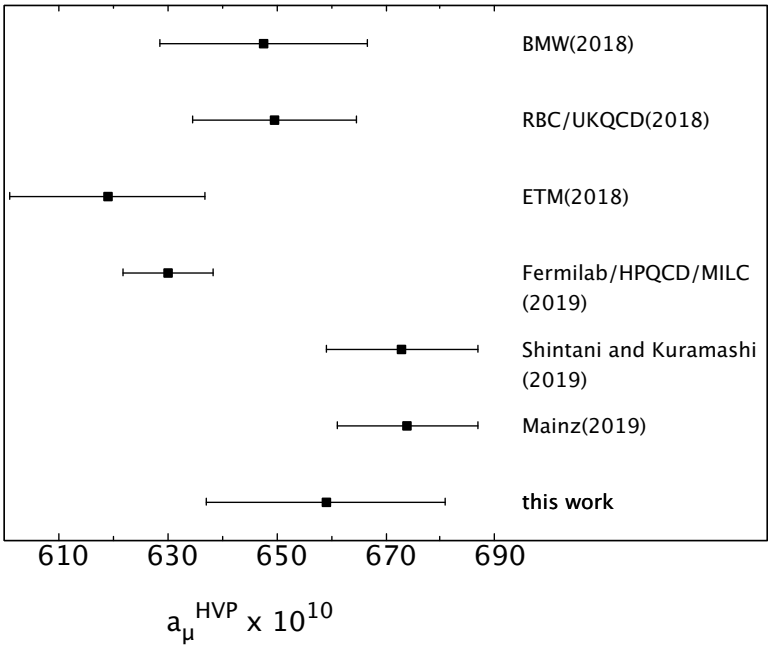

Figure 3.4: Contributions to the muon anomaly from the connected light quark vacuum polarization from recent publications [2] (BMW), [3] (RBC/UKQCD), [4] (ETM), [5] (Fermilab/HPQCD/MILC), [6] (Shintani and Kuramashi), [7] (Mainz).

The window method of Ref. [3] is used to make more precise comparisons with others since it focuses on medium-time-distance region where the results are more precise. The method sets up a "window" to choose which part of the integrand is considered in the a_μ, and it reads:

$$a_\mu^W = 2\sum_{t=0}^{T/2} C(t)w(t)(\Theta(t,t_0,\Delta) - \Theta(t,t_1,\Delta)) \tag{3.34}$$

$$\Theta(t,t',\Delta) = \frac{1}{2}(1+\tanh((t-t')/\Delta)), \tag{3.35}$$

where $t_1 - t_0$ is the size of the window and Δ denotes the width of the edges. We apply three different parameters of (t_0, t_1, Δ) to both two weighting functions and the results are

showed in Tab. 3.4. Several continuum limits with window setup $(t_0, t_1, \Delta) = (0.4, 1.0, 0.15)$ are plotted in Fig. 3.5, which include uncorrected data points with weighting functions w and $\hat{w}$, and taste-breaking corrected to NLO data points with w. The statistical errors are very small in this window setup, making it precise to understand the discretization effects. Due to the negligible effect, we ignore the pion mass and finite-volume corrections. However we still add in the taste-breaking corrections in one data plot, since it is still noticeable in nonzero lattice spacing. In continuum limits, these three plots are consistent. Furthermore, we also fit the data points including an a^4 term to get the continuum limits.

a (fm)	window 1	window 2	window 3	window 1($\hat{w}$)	window 2($\hat{w}$)	window 3 ($\hat{w}$)
0.12121(64)	201.07(56)	186.43(51)	308.32(94)	194.12(55)	179.32(49)	300.20(93)
0.08787(46)	205.95(66)	191.89(69)	319.16(1.44)	202.22(65)	187.95(68)	314.79(1.42)
0.05684(30)	207.13(92)	193.91(1.02)	324.37(2.40)	205.55(91)	192.18(1.02)	322.52(2.39)
0	209.78(96)	196.82(1.03)	329.99(2.25)	209.69(95)	196.52(1.02)	329.85(2.24)

Table 3.4: HVP contributions to the muon anomaly, in units of 10^{-10}, from the window method with windows 1, 2, and 3, $(t_0, t_1, \Delta) = (0.4, 1.0, 0.15)$, (0.4,1.0,0.3), and (0.4,1.3,0.15), respectively. $\hat{w}$ refers to the weighting function (3.18) in Eq. (3.15).

We also compare the R-ratio result of Ref. [8], as well as the resent results from RBC/UKQCD, who used domain wall fermions (DWF) [3]. As shown in Fig. 3.6, the HISQ result is above the DWF and R-ratio one, and the differences are about 1-2 percent of the total $a_\mu^{\rm HVP}$, so it is hard to say if it is a significant discrepancy. If we ignore the largest lattice spacing and do the extrapolation, the central value becomes lower with larger statistical errors.

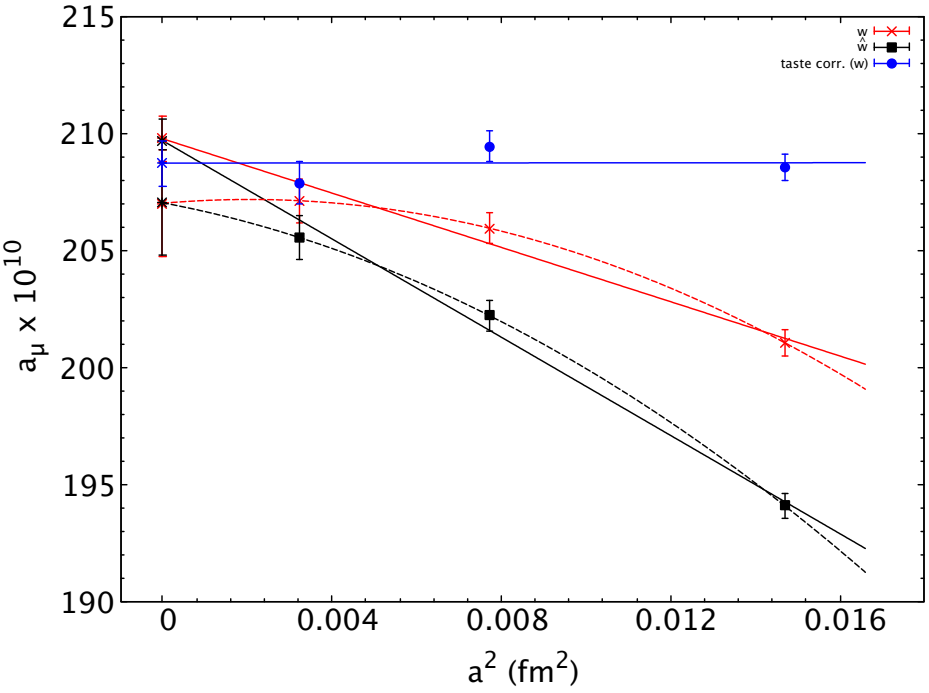

Figure 3.5: Continuum limit combined with the window method for lattice data without finite volume corrections. $t_0 = 0.4$ fm, $t_1 = 1$ fm, $\Delta = 0.15$. Squares (crosses) correspond to uncorrected data points with weighting function $\hat{w}$ (w); filled circles are taste-breaking corrected to NLO from w data points. Solid curves show linear fits in a^2; all three agree very well in the continuum limit. Dashed curves denote a fully constrained parametrization (no degrees of freedom) using both a^2 and a^4 terms.

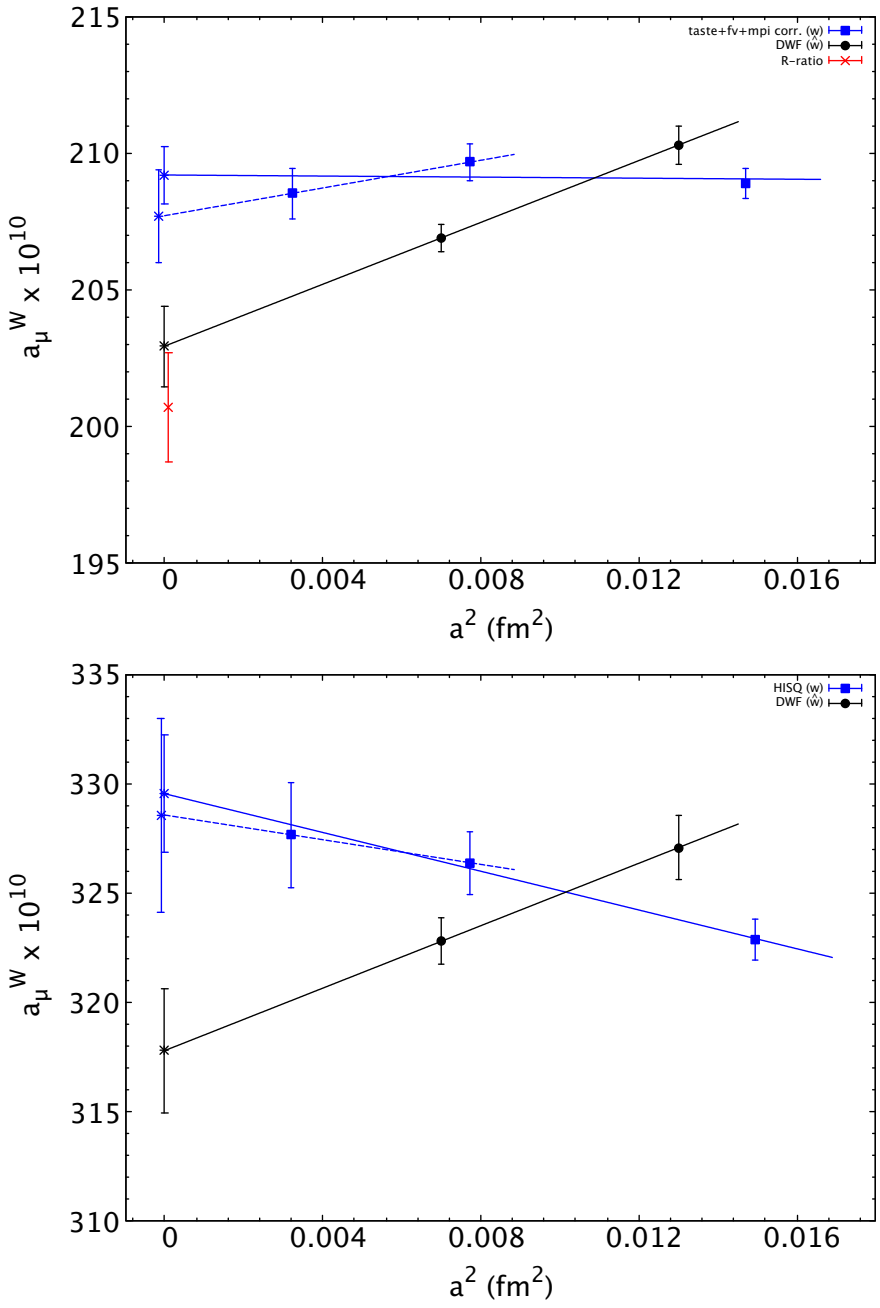

Figure 3.6: Continuum limit combined with the window method for DWF [3], using the weight $\hat{w}$ (circles) and HISQ, using the weight w (squares). $\Delta = 0.15$, $t_0 = 0.4$ fm, $t_1 = 1$ fm (upper panel) and 1.3 fm (lower panel). The R-ratio result (cross, using data from Ref. [8] by C. Lehner) is also shown in the upper panel. Finite volume (DWF and HISQ) and taste breaking (HISQ) corrections have been included to NLO in ChPT. Lattice spacing uncertainties, added in quadrature with statistical errors, are also included.

Chapter 4

π^0 exchange in the long-distance HLbL contribution to $g_\mu - 2$

4.1 The motivation of studying long-distance HLbL from π^0 pole

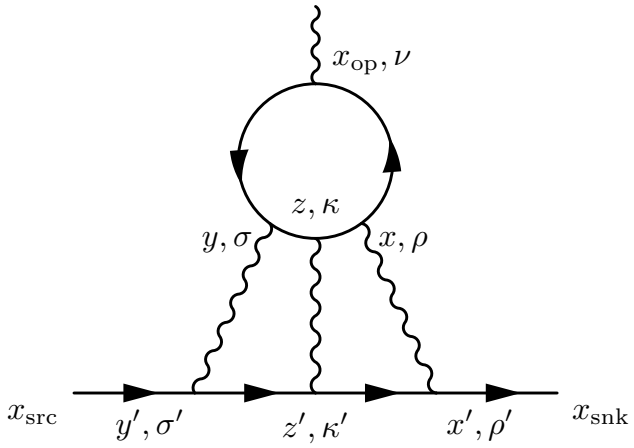

Figure 4.1: The connected light-by-light diagram. There are five other diagrams like this that corresponding to distinct ways of connecting the photons to the muon line.

The master formulae to obtain the connected hadronic light-by-light contribution to the $g-2$ is given by the electromagnetic Pauli form factor evaluated at zero momentum transfer,

$F_2(q^2=0)$, from the lattice calculation [39, 40],

$$\frac{F_2^{\rm cHLbL}(q^2=0)}{m}\frac{(\sigma_{s',s})_i}{2} = \frac{1}{VT}\sum_{x,y,z}\sum_{x_{\rm op}}\Big(\frac{1}{2}\epsilon_{i,j,k}(x_{\rm op}-x_{\rm ref})_j \cdot i\bar{u}_{s'}(\vec{0})\mathcal{F}_k^C(x,y,z,x_{\rm op})u_s(\vec{0})\Big), \tag{4.1}$$

where $(\sigma_{s',s})_i = \bar{u}_{s'}(\vec{0})\Sigma_i u_s(\vec{0})$ are the conventional Pauli matrices. The coordinated $x_{\rm op}$, x, y, z are the locations of the electromagnetic currents on the quark loop (see Fig. 4.1). In order to reduce the statistical noise in the Monte Carlo integration, we set $x_{\rm ref} = (\mathrm{x} + \mathrm{y})/2$ with the fact that the point $x_{\rm ref}$ can be chosen arbitrarily. By further manipulating the Eq. (4.1) to take advantage of the symmetry between x, y and z, we obtain

$$\frac{F_2^{\rm cHLbL}(q^2=0)}{m}\frac{(\sigma_{s',s})_i}{2} = \sum_{r,\tilde{z}}\mathfrak{Z}(\frac{r}{2},-\frac{r}{2},\tilde{z})\sum_{\tilde{x}_{\rm op}}\frac{1}{2}\epsilon_{i,j,k}(\tilde{x}_{\rm op})_j \cdot i\bar{u}_{s'}(\vec{0})\mathcal{F}_k^C(\frac{r}{2},-\frac{r}{2},\tilde{z},\tilde{x}_{\rm op})u_s(\vec{0}), \tag{4.2}$$

where $\mathfrak{Z}$ is defined as

$$\mathfrak{Z}(x,y,z) = \begin{cases} 3 & \text{if } |x-y| < |x-z| \quad \text{and} \quad |x-y| < |y-z| \\ 3/2 & \text{if } |x-y| = |x-z| < |y-z| \quad \text{or} \quad |x-y| = |y-z| < |x-z| \\ 1 & \text{if } |x-y| = |x-z| = |y-z| \\ 0 & \text{otherwise.} \end{cases} \tag{4.3}$$

The amplitude $\mathcal{F}_k^C(x,y,z,x_{\rm op})$ is given by

$$\mathcal{F}_k^C(x,y,z,x_{\rm op}) = (-ie)^6\mathcal{G}_{\rho,\sigma,\kappa}(x,y,z)\mathcal{H}^C_{\rho,\sigma,\kappa,\nu}(x,y,z,x_{\rm op}), \tag{4.4}$$

where $i^4\mathcal{H}^C_{\rho,\sigma,\kappa,\nu}(x,y,z,x_{\rm op})$ represents the four-point hadronic correlation function, and $i^3\mathcal{G}_{\rho,\sigma,\kappa}(x,y,z)$ is the QED weighting function. The connected diagram of $i^4\mathcal{H}^C_{\rho,\sigma,\kappa,\nu}(x,y,z,x_{\rm op})$ is given by

$$\mathcal{H}^C_{\rho,\sigma,\kappa,\nu}(x,y,z,x_{\rm op}) = \frac{1}{6}\mathcal{H}_{\rho,\sigma,\kappa,\nu}(x,y,z,x_{\rm op}) + \text{five other permutations of } x,\ y \text{ and } z, \tag{4.5}$$

where

$$\mathcal{H}_{\rho,\sigma,\kappa,\nu}(x,y,z,x_{\rm op}) = \sum_{q=u,d,s} (e_q/e)^4 \big\langle -{\rm tr}[i\gamma_\rho S_q(x,z) i\gamma_\kappa S_q(z,y) i\gamma_\sigma S_q(y,x_{\rm op}) i\gamma_\nu S_q(x_{\rm op},x)] \big\rangle_{\rm QCD}. \tag{4.6}$$

and $S_q(x,y)$ denotes the quark propagator.

In Ref. [41], both $i^4\mathcal{H}^C_{\rho,\sigma,\kappa,\nu}(x,y,z,x_{\rm op})$ and $i^3\mathcal{G}_{\rho,\sigma,\kappa}(x,y,z)$ are evaluated on a finite size lattice. However, if one switch to evaluate the QED weight function $\mathcal{G}$ in infinite-volume, which eliminates all the power-law like finite volume error, the statistical error becomes much larger. The large statistical error mostly come from the long-distance region, where $|x-y|$ is large. Also, at long distance, the four point function directly evaluated on the lattice suffers from significant QCD finite volume effects, although it is exponentially suppressed, the exponent is not very large due to the small pion mass. Fortunately, we can exploit the fact that, at long distance, the hadronic four point function is dominated by contribution from a single π^0 exchange. The aim of this paper is to treat the contribution from a single π^0 exchange at large $|x-y|$ in a different way, in order to avoid the large QCD finite volume effect in a direct calculation, and also to reduce the statistical error.

To achieve this, we replace the four-current connected Green's function $i^4\mathcal{H}^C_{\rho,\sigma,\kappa,\nu}(x,y,z,x_{\rm op})$ with π^0 contribution Green's function $\mathcal{A}^{\pi^0}_{\rho,\sigma,\kappa,\nu}(x,y,z,x_{\rm op})$ with the product of two $\pi^0\gamma\gamma$ amplitudes, each coupling a pair of currents to an on-shell π^0. These two amplitudes are joined by a pion propagator and all amplitudes are expressed in position space so they can be directly inserted in the standard, position-space evaluation of the HLbL amplitude. For the two $\pi^0\gamma\gamma$ vertex in position space, they can be calculated directly and individually in two different gauge configurations on the lattice. And since the pion propagator can be computed numerically for arbitrary source-sink distance, the whole amplitude of the pion pole contribution can be actually living in a infinite lattice volume.

4.2 Evaluation strategy

We begin with the Minkowski space four-current connected Green's function,

$$i^4\mathcal{H}^C_{\mu,\mu',\nu,\nu'}(x,x',y,y') = \big\langle 0\big|T\big(J_\mu(x)J_{\mu'}(x')J_\nu(y)J_{\nu'}(y')\big)\big|0\big\rangle, \tag{4.7}$$

where $J_\mu = \sum_{f=u,d,s} Q_f \overline{\psi}_f \gamma_\mu \psi_f$ is the hadronic part of the electromagnetic current. We will choose x and x' close to each other as are y and y'. However, we will assume that the (x,x') pair is far from the (y,y') pair. Define

$$\widetilde{x} = x' - x \tag{4.8}$$

$$\widetilde{y} = y' - y. \tag{4.9}$$

We now follow the usual steps to obtain a variant of the Källen-Lehman representation but keep only the single π^0 intermediate state since, as the lightest particle, its exchange will dominate this Green's function when x and y are far separated,

$$\begin{aligned}\mathcal{A}^{\pi^0,M}_{\mu\mu'\nu\nu'}(x,x',y,y') &= \frac{1}{(2\pi)^3}\int \frac{d^3p}{2E_\pi(p)} \\ &\Big\{\theta(x-y)\big\langle 0\big|T\big(J_\mu(x)J_{\mu'}(x')\big)\big|\pi^0(\vec{p})\big\rangle\big\langle\pi^0(\vec{p})\big|T\big(J_\nu(y)J_{\nu'}(y')\big)\big|0\big\rangle \\ &\quad +\theta(y-x)\big\langle 0\big|T\big(J_\nu(y)J_{\nu'}(y')\big)\big|\pi^0(\vec{p})\big\rangle\big\langle\pi^0(\vec{p})\big|T\big(J_\mu(x)J_{\mu'}(x')\big)\big|0\big\rangle\Big\},\end{aligned} \tag{4.10}$$

where the superscript π^0 indicates that only the π^0 contribution to the four-current connected Green's function is represented.

Next we use four-dimensional translational invariance to remove the variables x and y from the four current-current-π^0 amplitudes. We will also replace these four Lorentz-covariant current-current-π^0 amplitudes by functions of the four momentum p_α. Given the factors of $\exp(ip\cdot x)$ and $\exp(ip\cdot y)$ which appear, we can then replace the four vector p_α by

$-i\partial/\partial x_\alpha$ or $-i\partial/\partial y_\alpha$ as needed. For example we will replace

$$\begin{aligned}
&\left\langle 0\middle|T\left(J_\mu(x)J_{\mu'}(x')\right)\middle|\pi^0(\vec{p})\right\rangle \\
&\qquad = \left\langle 0\middle|T\left(J_\mu(0)J_{\mu'}(\widetilde{x})\right)\middle|\pi^0(\vec{p})\right\rangle e^{ip\cdot x} \\
&\qquad = \mathcal{F}_{\mu\mu'}(\widetilde{x}, p_\alpha)e^{ip\cdot x} \\
&\qquad = \mathcal{F}_{\mu\mu'}\left(\widetilde{x}, -i\frac{\partial}{\partial x_\alpha}\right)e^{ip\cdot x}. \qquad (4.11)
\end{aligned}$$

Using this approach to remove the explicit dependence of the four amplitudes on p_α, we can then perform the final step of the usual Källen-Lehman derivation and introduce the free pion propagator

$$\begin{aligned}
&\frac{1}{(2\pi)^3}\int\frac{d^3p}{2E_\pi(\vec{p})}\left\{\theta(x_0-y_0)e^{ip\cdot(x-y)}+\theta(y_0-x_0)e^{ip\cdot(y-x)}\right\} \\
&\qquad = \frac{i}{(2\pi)^4}\int d^4p\frac{e^{ip\cdot(x-y)}}{p_0^2-\vec{p}^{\,2}-M_\pi^2+i\epsilon} \\
&\qquad = \Delta_F(x-y, M_\pi), \qquad (4.12)
\end{aligned}$$

where $\Delta_F(x-y, M_\pi)$ is the free Minkowski-space propagator for a scalar particle of mass M_π.

In the final step, we can rewrite Eq. (4.10) in terms of $\mathcal{F}$ and Δ_F,

$$\mathcal{A}^{\pi^0,M}_{\mu\mu'\nu\nu'}(x,x',y,y') = \mathcal{F}_{\mu\mu'}\left(\widetilde{x}, -i\frac{\partial}{\partial x_\alpha}\right)\mathcal{F}_{\nu\nu'}\left(\widetilde{y}, i\frac{\partial}{\partial y_\alpha}\right)\Delta_F(x-y, M_\pi). \qquad (4.13)$$

Note, we have introduced erroneous terms where the derivative acts on a theta function which also depend on x and y. However, these are contact terms which vanish unless $x = y$ and so do not contribute to the large $x - y$ limit of interest here.

Since we are developing formulae that are to be used in a lattice calculation, we need to perform a Wick rotation and re-interpret our results as relations between Euclidean Green's functions. This standard procedure simultaneously rotates the phase of the time component

of position, $(\vec{x},t)$ and momentum, $(\vec{p},E)$, four-vectors by $e^{i\phi}$ where ϕ increases from 0 to $\pi/2$ as one moves from Minkowski space to Euclidean space. Dot products between two four-vectors, *e.g.* $\vec{x}\cdot\vec{p}-tE \rightarrow \vec{x}\cdot\vec{p}+tE$ after this rotation and constant quanties such as the Dirac γ matrices must be redefined using Euclidean versions to include the extra factor of i. Thus, Eq. (4.13) takes on the identical form,

$$\mathcal{A}^{\pi^0,E}_{\mu\mu'\nu\nu'}(x,x',y,y') = \mathcal{F}_{\mu\mu'}\left(\widetilde{x},-i\frac{\partial}{\partial x_\alpha}\right)\mathcal{F}_{\nu\nu'}\left(\widetilde{y},i\frac{\partial}{\partial y_\alpha}\right)\Delta_F(x-y,M_\pi), \tag{4.14}$$

where all the variables are now Euclidean vectors and an extra i has been removed from each of the time components of the four current four-vectors so that they become conventional E&M currents in Euclidean space.

In order to make Eq. (4.14) useful in a lattice calculation, the amplitudes $\mathcal{F}_{\mu\mu'}\left(\widetilde{x},-i\frac{\partial}{\partial x_\alpha}\right)$ must be written in an explicit Euclidean form that can be evaluated in a Feynman path integral. This can be done by applying the procedure followed above to the Minkowski-space Green's function

$$\mathcal{B}^{\mathcal{M}}_{\mu\mu'}(x,x',z) = \big\langle 0\big|T\big(J_\mu(x)J_{\mu'}(x')\pi^0(z)\big)\big|0\big\rangle, \tag{4.15}$$

where $\pi^0(z)$ is an interpolating operator for the π^0. We can repeat the steps that were used to transform Minkowski-space definition given in Eq. (4.7) into the Euclidean-space expression given in Eq. (4.14) and obtain the pion-pole contribution to $\mathcal{B}$, expressed in Euclidean-space,

$$\mathcal{B}^{\pi^0,E}_{\mu\mu'}(x,x',z) = \mathcal{F}_{\mu\mu'}\left(\widetilde{x},-i\frac{\partial}{\partial x_\alpha}\right)Z^{1/2}_{\pi^0}\Delta_F(x-z,M_\pi),$$

where Z_{π^0} is the wavefunction renormalization factor associated with the interpolating operator $\pi^0(x)$,

$$Z^{1/2}_{\pi^0} = \big\langle\pi^0\big|\pi^0(0)\big|0\big\rangle. \tag{4.16}$$

The steps required to obtain Eq. (4.16) follow closely those needed for Eq. (4.14). We need

only replace the relatively complex current-current operator $J_\nu(y)J_{\nu'}(y')$ by the simpler pion interpolating operator $\pi^0(z)$.

So far all of the steps taken have been exact. We expect the quantity computed, the contribution of a single pion exchange, to dominate the long distance limit in which $|x-y|$ in the case of Eq. (4.14) or $|x-z|$ in the case of Eq. (4.16) is large. Now we will evaluate the derivatives with respect to x and y which appear in these equations but keep only the leading term in an expansion powers of $1/L$. For example, to leading order in $1/|x-y|$,

$$\begin{aligned}\prod_{i=1}^{N}\left(\frac{\partial}{\partial x_{\rho_i}}\right)\Delta_F(x-y) &= \prod_{i=1}^{N}\left(\frac{\partial}{\partial x_{\rho_i}}\right)\frac{ce^{-|x-y|M_\pi}}{|x-y|^{3/2}} \\ &\approx \prod_{i=1}^{N}\left(-M_\pi\frac{(x-y)_{\rho_i}}{|x-y|}\right)\frac{ce^{-|x-y|M_\pi}}{|x-y|^{3/2}}.\end{aligned} \tag{4.17}$$

Inserting this approximation into Eqs (4.14) and (4.16), we obtain

$$\mathcal{A}^{\pi^0,E}_{\mu\mu'\nu\nu'}(x,x',y,y') = \mathcal{F}_{\mu\mu'}\left(\widetilde{x}, iM_\pi\hat{n}_\alpha\right)\mathcal{F}_{\nu\nu'}\left(\widetilde{y}, -iM_\pi\hat{n}_\alpha\right)\Delta_F(x-y,M_\pi) \tag{4.18}$$

$$\mathcal{B}^{\pi^0,E}_{\mu\mu'}(x,x',z) = \mathcal{F}_{\mu\mu'}\left(\widetilde{x}, iM_\pi\hat{n}_\alpha\right)Z^{1/2}_{\pi^0}\Delta_F(x-z,M_\pi), \tag{4.19}$$

where $\hat{n}_\alpha$ is the Euclidean unit vector $\frac{(x-y)_\alpha}{|x-y|}$.

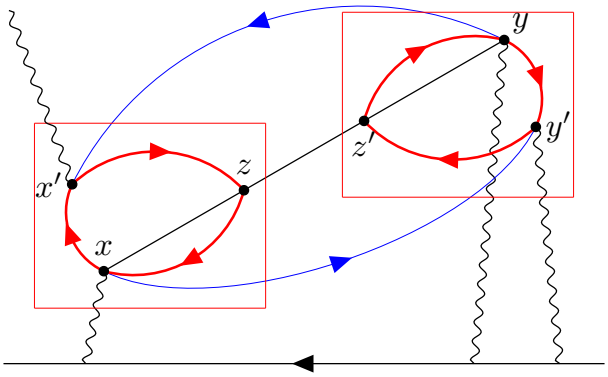

Figure 4.2: The diagram of long-distance HLbL contribution to the muon $g-2$ associate with π^0 exchange and two three-point amplitudes.

Finally we can obtain the equation of interest by combining these two results,

$$\mathcal{A}^{\pi^0,E}_{\mu\mu'\nu\nu'}(x,x',y,y') = \mathcal{B}^{\pi^0,E}_{\mu\mu'}(x,x',z)\mathcal{B}^{\pi^0,E}_{\nu\nu'}(y,y',z') \cdot\frac{1}{Z_{\pi^0}}\frac{\Delta_F(x-y,M_\pi)}{\Delta_F(x-z,M_\pi)\Delta_F(z'-y,M_\pi)}, \tag{4.20}$$

and the corresponding diagram is in Fig. 4.2. Since the two quantities $\mathcal{B}^{\pi^0,E}_{\mu\mu'}(x,x',z)$ and $\mathcal{B}^{\pi^0,E}_{\nu\nu'}(y,y',z')$ can be evaluated as independent lattice QCD configuration averages, the expression on the right hand side of Eq. (4.20) can be directly evaluated by a standard lattice QCD ensemble average allowing a direct calculation of the π^0 contribution to the long distance part the HLbL amplitude.

In such a complete calculation the points x, x', y and y' must be averaged over two, far-separated regions. For example we might average over all points obeying,

$$|x-y| \geq R_{\min} \quad \text{and} \quad \widetilde{x},\widetilde{y} \leq R_{\max}. \tag{4.21}$$

We note that the distance between the two π^0 vertices, $|x-y|$, in the HLbL Green's function does not constrain the separations used to compute the two current-current-π^0 vertices, $x-z$ and $z'-y$. These distances need only be large enough to accurately project onto the π^0 state and need not be as large as the distances of interest in studying the volume dependence of the HLbL calculation.

4.3 From point-source propagator to wall-source propagator

We firstly try to evaluate three-point functions $\mathcal{B}$ in Eq.(4.15) in lattice configurations and for each $\mathcal{B}$, two point-source propagators from the lattice should be chosen for the evaluation. In order to evaluate F_2, we sample several pairs of (x,y) across infinity position-space, therefor

the directions from x to y will be random. However, due to the fact that in practice, the source points of the propagators which are already evaluated are also randomly sampled in each lattice configuration, it is hard to find such available pair propagators ((x, z) for instance) which direction is exactly the same with direction of (x, y). Furthermore, it is even harder to apply AMA to improve the statistic.

Due to the concern above, we find a better way to implement on the lattice calculation. Instead of using point-source propagator, in which $\pi^0(z) = \overline{\psi}(z)\gamma_5\psi(z)$ of Eq. (4.15), we use wall-source propagator, in which the pion wall operator is defined as,

$$\pi^0_W(t) = \sum_{\vec{x},\vec{y}} \overline{\psi}(\vec{x}, t)\gamma_5\psi(\vec{y}, t) \tag{4.22}$$

and the two-point-wall correlation function we actually compute on the lattice becomes,

$$\mathcal{B}^W_{\mu_W\mu'_W}(0, \widetilde{x}', t_W) = \big\langle 0|J_{\mu_W}(0)J_{\mu'_W}(\widetilde{x}')\pi^0_W(t_W)|0\big\rangle. \tag{4.23}$$

There are some benefits by using the wall-source propagator. Firstly, the wall located on the π^0 side can have better representation of zero momentum π^0. Secondly, the average of two-point-wall amplitude can be evaluated in each lattice configurations to improve the statistics. Furthermore, AMA correction of $\mathcal{B}^W$ can be easily implemented.

In order to write Eq. (4.18) in terms of $\mathcal{B}^W_{\mu_W\mu'_W}(0, \widetilde{x}', t_W)$, we need several steps including inserting finite volume π^0 intermediate state and using Lorentz rotation transformation. Firstly, we consider such matrix element, in which two-current project into zero momentum π^0 state,

$$\big\langle 0|J_{\mu_W}(0)J_{\mu'_W}(\widetilde{x}')|\pi(\vec{p} = 0)\big\rangle = \mathcal{F}_{\mu_W\mu'_W}(\widetilde{x}', iM_\pi\hat{n}_t) \tag{4.24}$$

where $\mathcal{F}_{\mu_W\mu'_W}$ has the same meaning with the one showed in Eq. (4.18), but only in t direction. To rotate to the same direction of $(y-x)$, a Lorentz transformation operator Λ is introduced

as,

$$\hat{n}_\alpha = \Lambda(\hat{n}_\alpha, \hat{n}_t)\hat{n}_t, \tag{4.25}$$

which will rotate $\mathcal{F}_{\mu_W \mu'_W}$ to the direction of $(y - x)$,

$$\mathcal{F}_{\mu\mu'}(\widetilde{x}, iM_\pi \hat{n}_\alpha) = \Lambda_{\mu\mu_W}(\hat{n}_\alpha, \hat{n}_t)\Lambda_{\mu'\mu'_W}(\hat{n}_\alpha, \hat{n}_t)\mathcal{F}_{\mu_W \mu'_W}(\widetilde{x}', iM_\pi \hat{n}_t). \tag{4.26}$$

Secondly, we build bridge between $\mathcal{B}^W_{\mu_W \mu'_W}(0, \widetilde{x}', t_W)$ and $\mathcal{F}_{\mu_W \mu'_W}(\widetilde{x}', iM_\pi \hat{n}_t)$ by inserting finite volume π^0 intermediate state $|\pi^0(\vec{p} = 0, L)\rangle\langle\pi^0(\vec{p} = 0, L)|$ to both of them,

$$\mathcal{B}^W_{\mu_W \mu'_W}(0, \widetilde{x}', t_W) = \big\langle 0|J_{\mu_W}(0)J_{\mu'_W}(\widetilde{x}')|\pi^0(\vec{p} = 0, L)\big\rangle \cdot Z_W^{1/2} e^{M_\pi |t_W|} \tag{4.27}$$

$$\mathcal{F}_{\mu_W \mu'_W}(\widetilde{x}', iM_\pi \hat{n}_t) = \big\langle 0|J_{\mu_W}(0)J_{\mu'_W}(\widetilde{x}')|\pi^0(\vec{p} = 0, L)\big\rangle \cdot Z_p^{-1/2}, \tag{4.28}$$

where we define

$$Z_W^{1/2} = \big\langle \pi^0(\vec{p} = 0, L)|\pi^0_W(0)|0\big\rangle, \tag{4.29}$$

which denote the matrix element between finite volume π^0 wall state at time zero and finite volume zero momentum π^0 state, and

$$Z_p^{1/2} = \big\langle \pi^0(\vec{p} = 0, L)|\pi^0(0)|0\big\rangle = \frac{1}{\big\langle \pi^0(\vec{p} = 0, L)|\pi^0(\vec{p} = 0)\big\rangle}, \tag{4.30}$$

which denote the matrix element between infinite volume π^0 state in position space zero and finite volume zero momentum π^0 state.

Now, applying Eqs. (4.19)(4.28) back into Eq. (4.18), we obtain a formula in terms of

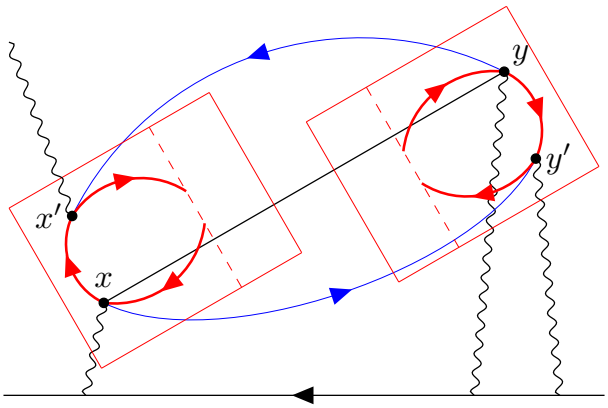

Figure 4.3: The diagram of long-distance HLbL contribution to the muon $g-2$ associate with π^0 exchange and two two-point-wall amplitudes.

two two-point-wall correlation functions,

$$\begin{aligned}\mathcal{A}^{\pi^0,E}_{\mu\mu'\nu\nu'}(x,x',y,y') = \Delta_F(x-y,M_\pi)\frac{1}{Z_{\pi^0}Z_W Z_p} \\ \times\frac{\Lambda_{\mu\mu_W}(\hat{n}_\alpha,\hat{n}_t)\Lambda_{\mu'\mu'_W}(\hat{n}_\alpha,\hat{n}_t)\mathcal{B}^W_{\mu_W\mu'_W}(0,\widetilde{x}',t_W)}{e^{-M_\pi|t_W|}} \\ \times\frac{\Lambda_{\nu\nu_W}(\hat{n}_\alpha,\hat{n}_t)\Lambda_{\nu'\nu'_W}(\hat{n}_\alpha,\hat{n}_t)\mathcal{B}^W_{\nu_W\nu'_W}(0,\widetilde{y}',t'_W)}{e^{-M_\pi|t'_W|}},\end{aligned} \tag{4.31}$$

Which associate with the diagram in Fig. 4.3. Finally, we still have two things left, Z_W and Z_p. For Z_W, we can find it through wall-to-wall correlation function by inserting finite volume zero momentum π^0 intermediate state,

$$\left\langle \pi^0_W(t)\pi^0_W(t')\right\rangle = Z_W e^{-M_\pi|t-t'|}. \tag{4.32}$$

And for Z_p, we consider such amplitude $\sum_{\vec{x}}\left\langle \pi(0)\pi(\vec{x},t)\right\rangle$ by inserting zero momentum π^0

intermediate state under finite volume and infinite volume,

$$\sum_{\vec{x}} \langle \pi(0)\pi(\vec{x},t) \rangle = \mathrm{L}^3 Z_p e^{-M_\pi |t|} \tag{4.33}$$

$$\sum_{\vec{x}} \langle \pi(0)\pi(\vec{x},t) \rangle = \frac{1}{2M_\pi} e^{-M_\pi |t|} \tag{4.34}$$

By comparing these two equations, we get

$$Z_p^{1/2} = \frac{1}{\sqrt{2M_\pi \mathrm{L}^3}}. \tag{4.35}$$

4.4 Computation details

The π^0 exchange in the long-distance HLBL calculation is performed on the 24^3, 32^3 and 48^3 physical-pion-mass ensemble generated by the RBC and UKQCD Collaborations. The details are described in Table 4.1. The whole calculation comes into two parts, evaluation of two-point-wall amplitudes $\mathcal{B}^W_{\mu_W \mu'_W}(0, \widetilde{x}', t_W)$ on each lattice configuration with AMA correction and computing F_2 using Eq. (4.2) by sampling the point-pairs (x, y).

Ensemble	a^{-1} (GeV)	am_π	Z_V^π	Z_W	N_{config}	$N_{\text{config-pair}}$	$(r_{\min}, r_{\text{mid}}, r_{\max})$	t_{sep}
24D	1.015	0.13975	0.72672	131683077	47	155	(5, 40, 60)	10
32D	1.015	0.139474	0.7260	319649623	43	80	(5, 40, 60)	10
32Dfine	1.378	0.10468	0.68339	772327306	69	103	(5, 55, 85)	14
48I	1.73	0.08049	0.71076	5082918150	24	31	(5, 70, 110)	16

Table 4.1: The parameters of each lattice ensemble

In the lattice computation for $\mathcal{B}^W_{\mu_W \mu'_W}(0, \widetilde{x}', t_W)$, point-source propagators and wall-source propagators are used. For point-source propagator, in each configuration, we randomly choose 256 spheres, which have radius 6, and four points are sampled uniformly within each sphere. Overall, 1024 points are sampled for each configuration. For wall-source propagator, all time slices are computed. To evaluate the the point-point-wall correlators, t_W is chosen as

$$t_W = \min(0, \widetilde{x}'_t) - t_{\text{sep}}, \tag{4.36}$$

which wall are always selected as a fixed distance t_{sep} to one of the two currents, which is closer to the wall in positive time direction.

Since the final $g-2$ from Eq. (4.31) involves two independent amplitudes evaluating two-point-wall correlation functions $\mathcal{B}^W_{\mu_W \mu'_W}(0, \widetilde{x}', t_W)$, they should come from two different configurations. We come up a jackknife method to estimate the statistical error of the $g-2$, which are computed from two independent lattice configurations.

In each lattice ensemble, we randomly pick $N_{\text{config-pair}}$ configuration pairs from the available configuration pool (N_{config}), and compute F_2 for each pair. In each jackknife subsample that omit the i-th configuration, only average F_2 from those pairs which are not include the i-th configuration. From the results of all jackknife subsamples, we can estimate the statistical error of F_2. The number of configurations and pairs for each lattice ensemble are described in Table 4.1.

After evaluation point-point-wall correlator $\mathcal{B}^W_{\mu_W \mu'_W}(0, \widetilde{x}', t_W)$ on the lattice, we need to sample the point-pair (x, y) in order to compute F_2. In each configuration combination, we sample 1024 point pairs in range $r_{\min} \leq r_L < r_{\max}$ in lattice units with the probability of choosing one particular relative distance r_L, which is

$$p(r_L) \propto \begin{cases} 1 & \text{if } r_{\min} \leq r_L < r_{\text{mid}} \\ 1/r_L^2 & \text{if } r_{\text{mid}} \leq r_L < r_{\max} \ , \end{cases} \tag{4.37}$$

an empirically suggested choice and the values of $(r_{\min}, r_{\text{mid}}, r_{\max})$ are in Table 4.1.

4.4.1 Position space model

The pion transition form factor was well studied on [42], which corresponding to the matrix element,

$$\left\langle 0 | T\big(iJ_\mu(u) iJ_\nu(v)\big) | \pi^0(\vec{p}) \right\rangle \tag{4.38}$$

and its momentum space representation

$$\int d^4u\ e^{-iq_1\cdot u - iq_2\cdot v}\big\langle 0|T\big(iJ_\mu(u)iJ_\nu(v)\big)|\pi^0(\vec{p})\big\rangle = \frac{1}{4\pi^2 F_\pi}\epsilon_{\mu\nu\rho\sigma}q_{1,\rho}q_{2,\sigma}F(q_1^2,q_2^2), \tag{4.39}$$

where q_1 and q_2 are the momenta of two photons and $p = q_1 + q_2$ is the on-shell pion momentum. Several models are considered to represent $F(q_1^2, q_2^2)$,

$$F^{\rm VMD}(q_1^2,q_2^2) = \frac{m_V^2}{q_1^2+m_V^2}\frac{m_V^2}{q_2^2+m_V^2} \tag{4.40}$$

$$F^{\rm TE}(q_1^2,q_2^2) = \frac{m_V^2/2}{q_1^2+m_V^2}\frac{m_V^2/2}{q_2^2+m_V^2} \tag{4.41}$$

$$F^{\rm LMD}(q_1^2,q_2^2) = \frac{8\pi F_\pi^2}{3m_V^2}F^{\rm TE}(q_1^2,q_2^2) + \big(1-\frac{8\pi F_\pi^2}{3m_V^2}\big)F^{\rm VMD}(q_1^2,q_2^2), \tag{4.42}$$

where m_V is set to the ρ meson mass. Eq. (4.40) is the vector meson dominance model (VMD) [43], Eq. (4.41) two end model (TE) and Eq. (4.42) lowest meson dominance model [44][45]. The LMD model which combined VMD and TE was chosen to be the model evaluation in this work. To implement this (taken the VMD model as the example), a position space of the VMD model is considered as

$$F(x,x',w) = m_V^4\Delta_{m_V}(x-w)\Delta_{m_V}(x'-w), \tag{4.43}$$

where $\Delta_{m_V}(x-y)$ denotes the propagator in position space. The matrix element tensor in position space can be obtained by replacing momenta to spacial operators,

$$F_{\mu\mu'}(x,x',w) = \frac{-i}{4\pi^2 F_\pi}\epsilon_{\mu\mu'\rho\sigma}(-i\partial_\rho^x)(-i\partial_\sigma^{x'})F(x,x',w). \tag{4.44}$$

The partial derivative is taken under discrete finite volume space-time and the volume parameters were shown in Table. 4.2. The two-point-wall amplitudes of Eq. (4.23) can be

size	a^{-1} (GeV)	am_π	Z_W	$(r_{\min}, r_{\mathrm{mid}}, r_{\max})$	t_{sep}
$24^3 \times 96$	1.0	0.134875	51093	(5, 40, 60)	24
$32^3 \times 128$	1.0	0.134875	121109	(5, 40, 60)	32
$32^3 \times 128$	1.3333	0.075896	161635	(5, 55, 85)	32
$48^3 \times 192$	1.0	0.134875	408741	(5, 40, 60)	48
$48^3 \times 192$	2.0	0.0337378	818880	(5, 70, 110)	48

Table 4.2: The parameters of each model ensemble

expressed by model

$$\mathcal{B}_{\mu\mu'}^{\pi^0,\mathrm{model}}(x, x', t) = -\int_{\vec{z}} \int_{w} F_{\mu\mu'}(x, x', w) \Delta_{m_\pi}(z - w). \tag{4.45}$$

By inserting back to Eq. (4.31), we can get F_2 computed from model.

4.5 Results

Following the procedure described above we can study the contribution to $g-2$ as a function of $r = \max(|x-y|, |x-y'|, |y-y'|)$, which denotes the partial sum of the contribution in distance range from the infinity to r. Since this calculation only focus on the long distance part of the contribution by π^0 exchange and the point-pairs of (x, y) were sampled larger than a distance, only large r in the plot should be considered.

The discretization error correction and finite volume effect correction are also applied. The continuum limits are computed by linear fits in a^2 between lattice ensembles 24D and 32Dfine. The finite volume effect correction are computed by the differences between lattice ensemble 24D and 32D, and 32D are thought to be the infinite volume comparing to 24D. The final correction with nonzero lattice spacing and finite volume effects are shown in Fig. 4.4. We select some r to show the results of long-distance HLbL contribution to the $g-2$ from π^0 exchange in Table. 4.3.

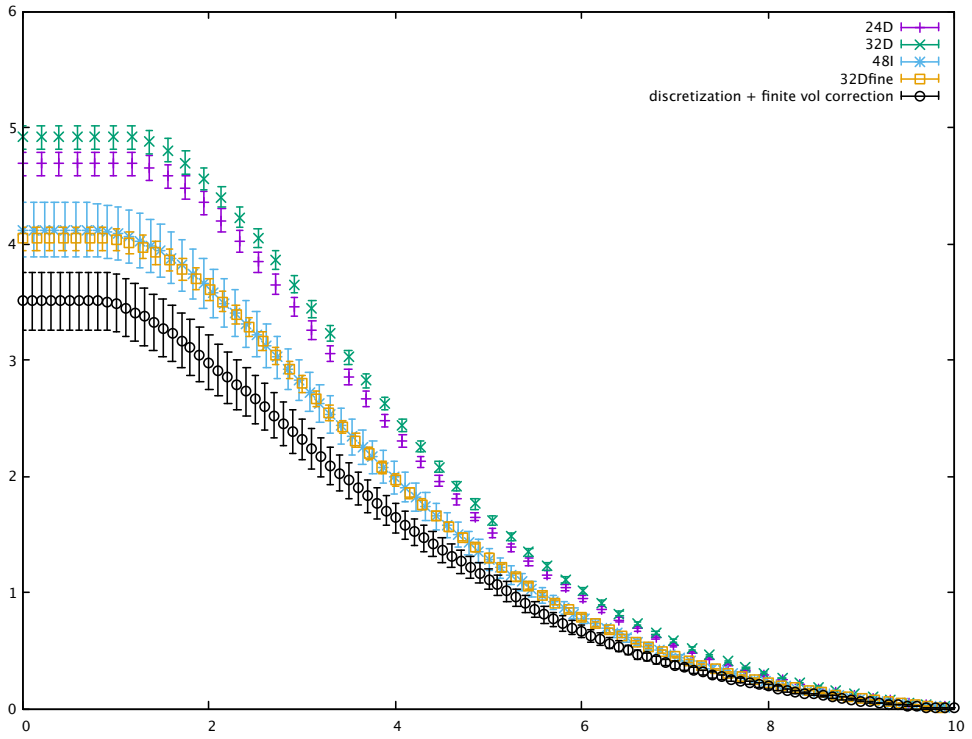

Figure 4.4: The π^0 exchange in the long-distance HLbL contribution to the muon $g-2$ from infinity to distance r (in unit of fm), and the $r = \max(|x-y|, |x-y'|, |y-y'|)$ denotes the longest distance between points x, y and y'. The non-zero lattice spacing correction are determined between the lattice ensemble 32Dfine and 24D and finite volume correction are determined between 32D and 24D.

Ensemble	$(g-2) \times 10^{10}$				
	$r = 2$ (fm)	$r = 2.5$ (fm)	$r = 3$ (fm)	$r = 3.5$ (fm)	$r = 4$ (fm)
24D	4.3(0.1)	3.87(0.09)	3.36(0.79)	2.85(0.07)	2.37(0.06)
32D	4.51(0.09)	4.07(0.09)	3.56(0.07)	3.02(0.07)	2.51(0.06)
32Dfine	3.60(0.09)	3.22(0.08)	2.80(0.07)	2.37(0.06)	1.97(0.05)
48I	3.6(0.2)	3.2(0.2)	2.7(0.2)	2.3(0.2)	2.0(0.1)
extrapolation DSDR	3.0(0.2)	2.8(0.2)	2.4(0.2)	2.0(0.1)	1.6(0.1)
extrapolation model	4.39(0.13)	3.94(0.13)	3.39(0.12)	2.89(0.11)	2.40(0.10)
pion pole model	5.725	4.771	3.827	3.026	2.403

Table 4.3: Lattice results of the π^0 exchange in the long-distance HLbL contribution to the muon $g-2$ from infinity to distance r. The non-zero lattice spacing and finite volume corrected results from the DSDR ensembles and model assumptions, and the results from pion pole model, are also shown in the last three lines.

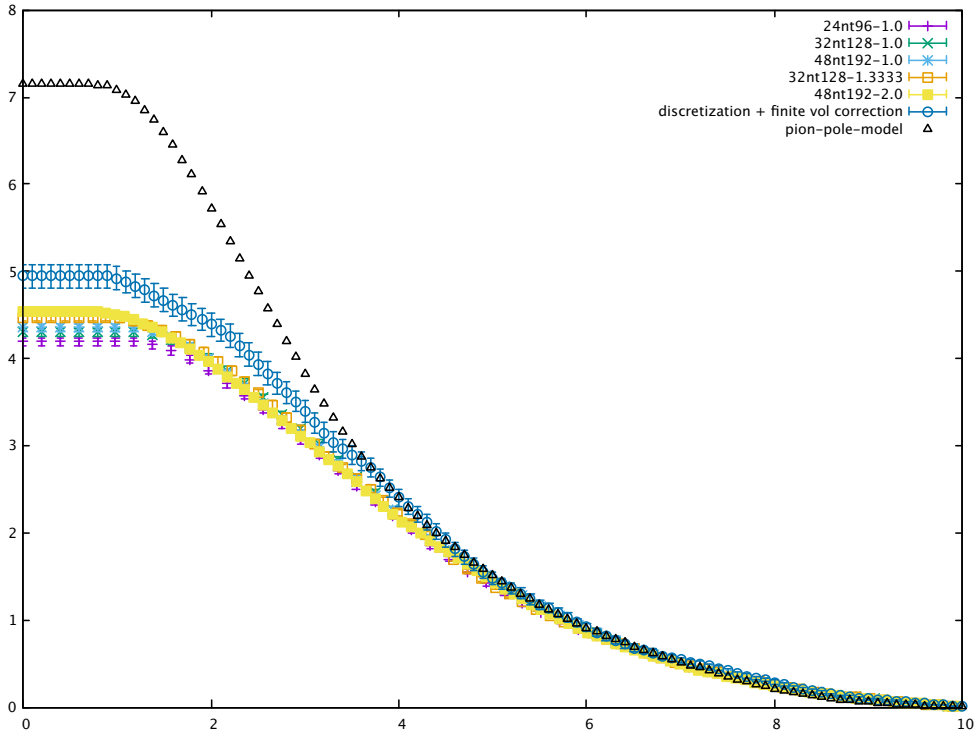

Figure 4.5: The same plots as Fig. 4.4 from model's prediction. The non-zero lattice spacing correction are determined between the model ensemble "32nt128-1.3333" and "24nt96-1.0" and finite volume correction are determined between "32nt128-1.0" and "24nt96-1.0".

Bibliography

[1] A. Bazavov et al. Charmed and light pseudoscalar meson decay constants from four-flavor lattice QCD with physical light quarks. *Phys. Rev.*, D90(7):074509, 2014.

[2] Sz. Borsanyi et al. Hadronic vacuum polarization contribution to the anomalous magnetic moments of leptons from first principles. *Phys. Rev. Lett.*, 121(2):022002, 2018.

[3] T. Blum, P. A. Boyle, V. Gulpers, T. Izubuchi, L. Jin, C. Jung, A. Juettner, C. Lehner, A. Portelli, and J. T. Tsang. Calculation of the hadronic vacuum polarization contribution to the muon anomalous magnetic moment. *Phys. Rev. Lett.*, 121(2):022003, 2018.

[4] D. Giusti, F. Sanfilippo, and S. Simula. Light-quark contribution to the leading hadronic vacuum polarization term of the muon $g-2$ from twisted-mass fermions. *Phys. Rev.*, D98(11):114504, 2018.

[5] C. T. H. Davies et al. Hadronic-vacuum-polarization contribution to the muon's anomalous magnetic moment from four-flavor lattice QCD. 2019.

[6] Eigo Shintani and Yoshinobu Kuramashi. Study of systematic uncertainties in hadronic vacuum polarization contribution to muon $g-2$ with 2+1 flavor lattice QCD. 2019.

[7] Antoine Gérardin, Marco Cè, Georg von Hippel, Ben Hörz, Harvey B. Meyer, Daniel Mohler, Konstantin Ottnad, Jonas Wilhelm, and Hartmut Wittig. The leading hadronic contribution to $(g-2)_\mu$ from lattice QCD with $N_\mathrm{f} = 2+1$ flavours of O(a) improved Wilson quarks. 2019.

[8] Alexander Keshavarzi, Daisuke Nomura, and Thomas Teubner. Muon $g-2$ and $\alpha(M_Z^2)$: a new data-based analysis. *Phys. Rev.*, D97(11):114025, 2018.

[9] Michael Creutz. *Quarks, gluons and lattices*. Cambridge Monographs on Mathematical Physics. Cambridge Univ. Press, Cambridge, UK, 1985.

[10] Tatsumi Aoyama, Masashi Hayakawa, Toichiro Kinoshita, and Makiko Nio. Complete Tenth-Order QED Contribution to the Muon g-2. *Phys.Rev.Lett.*, 109:111808, 2012.

[11] C. Gnendiger, D. Stöckinger, and H. Stöckinger-Kim. The electroweak contributions to $(g-2)_\mu$ after the Higgs boson mass measurement. *Phys.Rev.*, D88:053005, 2013.

[12] Kaoru Hagiwara, Ruofan Liao, Alan D. Martin, Daisuke Nomura, and Thomas Teubner. $(g-2)_\mu$ and alpha(M_Z^2) re-evaluated using new precise data. *J.Phys.*, G38:085003, 2011.

[13] Alexander Kurz, Tao Liu, Peter Marquard, and Matthias Steinhauser. Hadronic contribution to the muon anomalous magnetic moment to next-to-next-to-leading order. *Phys.Lett.*, B734:144–147, 2014.

[14] Joaquim Prades, Eduardo de Rafael, and Arkady Vainshtein. Hadronic Light-by-Light Scattering Contribution to the Muon Anomalous Magnetic Moment. 2009.

[15] G.W. Bennett et al. Final Report of the Muon E821 Anomalous Magnetic Moment Measurement at BNL. *Phys.Rev.*, D73:072003, 2006.

[16] Fred Jegerlehner and Andreas Nyffeler. The Muon g-2. *Phys. Rept.*, 477:1–110, 2009.

[17] R. M. Carey et al. The New (g-2) Experiment: A proposal to measure the muon anomalous magnetic moment to +-0.14 ppm precision. 2009.

[18] Tsutomu Mibe. New g-2 experiment at J-PARC. *Chin. Phys.*, C34:745–748, 2010.

[19] Kenneth G. Wilson. Confinement of quarks. *Physical Review D*, 10(8):2445–2459, 1974.

[20] Leonard Susskind. Lattice fermions. *Physical Review D*, 16(10):3031–3039, 1977.

[21] E. Follana, Q. Mason, C. Davies, K. Hornbostel, G. P. Lepage, J. Shigemitsu, H. Trottier, and K. Wong. Highly improved staggered quarks on the lattice, with applications to charm physics. *Phys. Rev.*, D75:054502, 2007.

[22] David B. Kaplan. Chiral Symmetry and Lattice Fermions. In *Modern perspectives in lattice QCD: Quantum field theory and high performance computing. Proceedings, International School, 93rd Session, Les Houches, France, August 3-28, 2009*, pages 223–272, 2009.

[23] Georg v. Hippel. Exactly chiral fermions. *BLOG: Life on the lattice*, 2006.

[24] Thomas Blum, Taku Izubuchi, and Eigo Shintani. New class of variance-reduction techniques using lattice symmetries. *Phys.Rev.*, D88(9):094503, 2013.

[25] Eigo Shintani, Rudy Arthur, Thomas Blum, Taku Izubuchi, Chulwoo Jung, and Christoph Lehner. Covariant approximation averaging. *Phys. Rev.*, D91(11):114511, 2015.

[26] Leonardo Giusti, P. Hernandez, M. Laine, P. Weisz, and H. Wittig. Low-energy couplings of QCD from current correlators near the chiral limit. *JHEP*, 04:013, 2004.

[27] Thomas A. DeGrand and Stefan Schaefer. Improving meson two point functions in lattice QCD. *Comput. Phys. Commun.*, 159:185–191, 2004.

[28] H. Neff, N. Eicker, T. Lippert, John W. Negele, and K. Schilling. On the low fermionic eigenmode dominance in QCD on the lattice. *Phys. Rev.*, D64:114509, 2001.

[29] Leonardo Giusti and Silvia Necco. Low-mode averaging for baryon correlation functions. *PoS*, LAT2005:132, 2006.

[30] Thomas Blum, Taku Izubuchi, and Eigo Shintani. New class of variance-reduction techniques using lattice symmetries. *Phys. Rev.*, D88(9):094503, 2013.

[31] B. e. Lautrup, A. Peterman, and E. de Rafael. Recent developments in the comparison between theory and experiments in quantum electrodynamics. *Phys. Rept.*, 3:193–259, 1972.

[32] Eduardo de Rafael. Hadronic contributions to the muon g-2 and low-energy QCD. *Phys. Lett.*, B322:239–246, 1994.

[33] T. Blum. Lattice calculation of the lowest order hadronic contribution to the muon anomalous magnetic moment. *Phys.Rev.Lett.*, 91:052001, 2003.

[34] David Bernecker and Harvey B. Meyer. Vector Correlators in Lattice QCD: Methods and applications. *Eur.Phys.J.*, A47:148, 2011.

[35] Christoph Lehner and Taku Izubuchi. Towards the large volume limit - A method for lattice QCD + QED simulations. *PoS*, LATTICE2014:164, 2015.

[36] Christopher Aubin, Thomas Blum, Peter Chau, Maarten Golterman, Santiago Peris, and Cheng Tu. Finite-volume effects in the muon anomalous magnetic moment on the lattice. *Phys. Rev.*, D93(5):054508, 2016.

[37] Christopher Aubin, Thomas Blum, Cheng Tu, Maarten Golterman, Chulwoo Jung, and Santiago Peris. Light quark vacuum polarization at the physical point and contribution to the muon $g-2$. *Phys. Rev.*, D101(1):014503, 2020.

[38] Peter Boyle, Azusa Yamaguchi, Guido Cossu, and Antonin Portelli. Grid: A next generation data parallel C++ QCD library. 12 2015.

[39] Thomas Blum, Norman Christ, Masashi Hayakawa, Taku Izubuchi, Luchang Jin, and Christoph Lehner. Lattice calculation of hadronic light-by-light contribution to the muon anomalous magnetic moment. 10 2015.

[40] Thomas Blum, Norman Christ, Masashi Hayakawa, Taku Izubuchi, Luchang Jin, Chulwoo Jung, and Christoph Lehner. Using infinite volume, continuum QED and lattice QCD for the hadronic light-by-light contribution to the muon anomalous magnetic moment. 2017.

[41] Thomas Blum, Norman Christ, Masashi Hayakawa, Taku Izubuchi, Luchang Jin, Chulwoo Jung, and Christoph Lehner. Connected and Leading Disconnected Hadronic Light-by-Light Contribution to the Muon Anomalous Magnetic Moment with a Physical Pion Mass. *Phys. Rev. Lett.*, 118(2):022005, 2017.

[42] Antoine Gérardin, Harvey B. Meyer, and Andreas Nyffeler. Lattice calculation of the pion transition form factor with $N_f = 2+1$ Wilson quarks. *Phys. Rev.*, D100(3):034520, 2019.

[43] *MesonNet Workshop on Meson Transition Form Factors*, 2012.

[44] B. Moussallam. Chiral sum rules for parameters of the order six Lagrangian in the W-Z sector and application to pi0, eta, eta-prime decays. *Phys. Rev.*, D51:4939–4949, 1995.

[45] M. Knecht, S. Peris, M. Perrottet, and E. de Rafael. Decay of pseudoscalars into lepton pairs and large N(c) QCD. *Phys. Rev. Lett.*, 83:5230–5233, 1999.